# Regime Change Behavior during Asian Monsoon Onset

RUTH GEEN, F. H. LAMBERT, AND G. K. VALLIS

*College of Engineering, Mathematics and Physical Sciences, University of Exeter, Exeter, United Kingdom*

(Manuscript received 24 February 2017, in final form 14 November 2017)

ABSTRACT

As the ITCZ moves off the equator on an aquaplanet, the Hadley circulation transitions from an equinoctial regime with two near-symmetric, significantly eddy-driven cells to a monsoon-like regime with a strong, thermally direct cross-equatorial cell, intense low-latitude precipitation, and a weak summer hemisphere cell. Dynamical feedbacks appear to accelerate the transition. This study investigates the relevance of this behavior to monsoon onset by using primitive equation model simulations ranging from aquaplanets to more realistic configurations with Earth's continents and topography. A change in the relationship between ITCZ latitude and overturning strength is identified once the ITCZ moves poleward of approximately 7°. Monsoon onset is associated with off-equatorial ascent in regions of nonnegligible planetary vorticity, and this is found to generate a vortex stretching tendency that reduces upper-level absolute vorticity. In an aquaplanet, this causes a transition to the cross-equatorial, thermally direct regime, intensifying the overturning circulation. Analysis of the zonal momentum budget suggests that a stationary wave, driven by topography and land–sea contrast, can trigger a similar transition in the more realistic model configuration, with the wave extending the ascent region of the Southern Hemisphere Hadley cell northward, and enhanced overturning then developing to the south. These two elements of the circulation resemble the East and South Asian monsoons.

## 1. Introduction

The onset of the Asian summer monsoon is characterized by a fast transition from a dry season, with easterly flow at lower levels and westerly flow at upper levels, to a wet season, with lower-level westerlies and upper-level easterlies. However, the dynamics involved are still not well understood. In this paper, we try to unify perspectives from previous studies of monsoon dynamics in aquaplanets and investigate the relevance of these to the real world.

The monsoon is forced by the seasonal cycle of solar heating, resulting in migration of the intertropical convergence zone (ITCZ) (Chao and Chen 2001) and warming of land relative to ocean (Li and Yanai 1996). Continents, orography, and sea surface temperature (SST) variations result in regional circulation features and different onset times across different longitudes (e.g., Wu and Wang 2001; Zhang et al. 2002). However, both models and observations indicate that the transition in the circulation during monsoon onset occurs faster than would be expected from the northward progression of the peak insolation (Yin 1949; Xie and Saiki 1999). This suggests that dynamical feedbacks may play an important role.

An emerging view in the literature is that monsoon onset marks a sharp transition between two dynamical regimes (e.g., Chao 2000). Considering the circulation on an aquaplanet, where the lower boundary conditions are zonally symmetric, the steady-state time-mean zonal momentum budget may be approximated as

$$\left(f-\frac{\partial\overline{u}}{\partial y}\right)\overline{v}-\frac{\partial\overline{u'v'}}{\partial y}=0, \tag{1}$$

where $f$ is the Coriolis parameter, and $u$ and $v$ are the zonal and meridional wind speeds, respectively. Overbars indicate the time mean, and primes indicate deviations from this. In the deep tropics eddy fluxes are generally assumed to be weak, so that the final term on the left-hand side of Eq. (1) is negligible. In this situation, two steady-state solutions exist: either the zonal

*Corresponding author*: Ruth Geen, rg419@exeter.ac.uk

DOI: 10.1175/JCLI-D-17-0118.1

mean meridional wind speed or the zonal mean absolute vorticity must be equal to zero. Eddies may then allow some deviation from these solutions. In an axisymmetric model with off-equatorial heating this can result in threshold behavior (Plumb and Hou 1992; Privé and Plumb 2007a,b). As the heating becomes stronger there is a change from a very weak meridional circulation (with $\overline{v}$ very small) to a stronger, thermally direct overturning cell (with absolute vorticity near the upper boundary now very small). This latter regime also corresponds to an angular momentum–conserving Hadley cell, as in Schneider (1977), Held and Hou (1980) and Lindzen and Hou (1988).

However, as has long been recognized (e.g., Pfeffer 1981; Kim and Lee 2001), eddy effects are almost certainly not negligible in the Hadley cell, especially near its poleward edge where the dynamics transition into a midlatitude regime. Relatedly, more recent work suggests that monsoon onset relates to a transition from a largely eddy-driven to an axisymmetric, cross-equatorial Hadley circulation. Bordoni and Schneider (2008) identified abrupt circulation changes, similar to those observed over monsoon onset, in idealized aquaplanet simulations, provided a sufficiently shallow mixed layer depth is used. They proposed that the development of upper-level easterlies in the summer hemisphere restricts the propagation of eddy activity in this region. The result is a more axisymmetric Hadley cell, which, from Eq. (1), will also have low upper-level absolute vorticity. Meanwhile, the lower branch of the cell advects cooler, drier air from the winter to summer hemisphere, up the temperature gradient. This pushes the maximum moist static energy, and the ITCZ, poleward. This extends the region of upper-level easterlies, preventing the penetration of eddy effects and giving a positive feedback. In their moist model, this regime change was accompanied by the onset of intense precipitation at low latitudes, which they connect to the monsoon. If a similar mechanism can be taken to apply in the real world, then the role of land is essentially to provide a surface with low thermal inertia, in which case temperature gradients associated with land–sea contrast are not necessary to trigger monsoon onset, although they may still be important in localizing the monsoon longitudinally, which is sometimes regarded as one of its defining features.

In reality the lower boundary condition on Earth is of course not symmetric, unlike the aquaplanet studies discussed above. To investigate the role played by stationary waves in the seasonal transition of the circulation, Shaw (2014) compared the circulation characteristics observed in ERA-Interim data with those induced when a prescribed wave is introduced into the SSTs. She identified a transition to a regime dominated by planetary-scale waves, which occurs once the amplitude of the SST wave is increased past a threshold value of 6 K. It was demonstrated that the stationary eddies involved were able to propagate even through regions of negative zonal velocity, as they are advected by the zonal mean meridional flow. This regime also exhibits low upper-level absolute vorticity locally, suggesting localized behavior similar to the aquaplanet thermally direct circulation. Zhai and Boos (2015) used a dry primitive equation model to investigate this behavior systematically. They compared the effect of steady, off-equatorial zonally symmetric and asymmetric forcings on the meridional circulation. As the zonal mean forcing amplitude was increased, a sudden change in the strength of the meridional circulation was identified and associated with low absolute vorticity in the upper branch of the Hadley cell. Asymmetric forcings introduced additional zonal overturning with a structure similar to that seen in Gill (1980). This was found to increase linearly in strength with the forcing amplitude, with no abrupt regime change apparent.

Regime change behavior has also been noted in observations. Krishnamurti and Ramanathan (1982) identified a sudden enhancement of the kinetic energy of the nondivergent flow during monsoon onset in observational data from the Global Atmospheric Research Program (GARP) summer Monsoon Experiment (MONEX). Analyzing the energy conversions during onset in numerical experiments, they find these to be sensitive to the structure of the diabatic heating field. The configuration of land, topography, and sea surface temperatures may therefore be important in determining the real-world monsoon dynamics.

Here we attempt to reconcile and unify the various mechanisms suggested above, and to link the processes discussed in these idealized studies to the dynamics of a more realistic setup, with a particular focus on the Asian monsoon systems. The bulk of work presented compares results from an aquaplanet with a mixed layer depth (MLD) of 2 m, with those from an experiment with idealized land in the shape of Earth's continents and topography. Where relevant, deeper MLD aquaplanets are used to illustrate behavior with a higher thermal inertia surface and for comparison with the high thermal inertia ocean in the more realistic experiment. Intermediate experiments, with various combinations of land and topography, are also used to fill the gap between the aquaplanets and more realistic experiment. The model used and experimental design are discussed in section 2. In section 3 we compare the overturning circulations of the aquaplanet and more realistic simulations over onset, and identify similarities in behavior consistent with a dynamical regime change. To understand the reduction in

upper-level absolute vorticity responsible for this change, the vorticity budget is analyzed in section 4. In section 5 the role of zonal asymmetry and stationary waves is investigated, giving insight into the limitations of aquaplanet experiments in describing the real world. Section 6 discusses the intermediate experiments, exploring the effects of land, topography, and ocean heat fluxes. Section 7 summarizes our results and discusses the implications for our understanding of monsoon onset.

## 2. Model and experiments

Experiments are run using "Isca," a framework for modeling both Earth and other planetary atmospheres based around the GFDL 2013 idealized model release, but extended to include configurable astronomy and land, and a range of parameterizations for diabatic heating. The setup here used is detailed in this section. For a full summary of the model, see Vallis et al. (2018).

Aside from an updated dynamical core, the particular configuration used is similar to Model of an Idealized Moist Atmosphere (MiMA; see Jucker and Gerber 2017). The model physics includes parameterizations of large-scale condensation, moist convection, vertical diffusion of heat, momentum and moisture, and radiative transfer. For all but the last of these, the parameterizations used are as in Frierson et al. (2006) and Frierson (2007), with the amendments of O'Gorman and Schneider (2008). Rather than using a gray atmosphere with prescribed optical depths, the Rapid Radiative Transfer Model (RRTM; Mlawer et al. 1997) has been coupled to the model. The radiative heating is recalculated every 3600 s of model time, compared with the 720-s time step used for the dynamics and other physical processes. Clouds are not included in the parameterization of moist processes or of radiation. Simulations are run at spectral T42 resolution, corresponding to approximately 2.8° resolution at the equator, with 40 unevenly spaced sigma levels. A slab ocean of prescribed mixed layer depth allows a closed atmospheric energy budget to be achieved. The temperature of the slab responds only to the incident fluxes at the sea surface, with no dynamic heat transport. A sponge layer is applied at the model top to inhibit unstable gravity wave–like behavior. Despite the idealized nature of our experiments, comparison of the model in its most realistic configuration with reanalysis (e.g., Kållberg et al. 2005) indicates that the key features of Earth's climatology are successfully captured. The appendix shows plots using data from the Global Precipitation Climatology Project (GPCP; Huffman et al. 2016) and from the European Centre for Medium-Range Weather Forecasts (ECMWF) interim reanalysis (ERA-Interim; ECMWF 2009) dataset, for comparison with the data presented in the main text of this study.

Land is incorporated into the model by varying mixed layer depth, albedo, roughness length, and moisture availability over prescribed areas. The latter is controlled by introducing a scaling parameter $\alpha$ into the equation for surface evaporation $E$:

$$E = \rho_a C |\mathbf{v}_a| (q_a - \alpha q_s), \tag{2}$$

where $\rho_a$, $|\mathbf{v}_a|$, and $q_a$ are the density, horizontal wind speed, and specific humidity at the lowest model level, respectively; $C$ is the drag coefficient; and $q_s$ is the saturation specific humidity at the surface temperature [cf. Eq. (11) in Frierson et al. 2006]; $\alpha$ acts as a scaling parameter to reduce the effective saturation specific humidity of the surface.

The simulations performed comprise three aquaplanet configurations, a configuration intended to resemble Earth, and three experiments with various combinations of land, topography, and ocean heat fluxes ($Q$ fluxes) to bridge the gap between the aquaplanets and more realistic configuration. Simulations are summarized in Table 1. Where included, land and topography are based on the ERA-Interim masks (Fig. 1). Topography is regularized following Lindberg and Broccoli (1996) to reduce the Gibbs ripples that arise from the truncated spherical harmonic expansion. The ocean is given a mixed layer depth of 20 m, while land has a depth of 2 m. For all experiments ocean is given an albedo of 0.25 and land an albedo of 0.325, with the high albedo values accounting for the lack of reflection by clouds in the model. Both ocean and land use a roughness length of $2 \times 10^{-4}$ m. A scale factor $\alpha$ of 0.7 is introduced to reduce evaporation over land, as in Eq. (2). The parameter values were chosen to provide a climate comparable to reanalysis. Sensitivity experiments in which the parameters were varied give similar climates and behavior to the experiments presented here.

In the more complex experiments, seasonally varying $Q$ fluxes are prescribed. These were derived from the Atmospheric Model Intercomparison Project (AMIP) SSTs following the methodology outlined in Russell et al. (1985). The resulting fluxes have a comparable structure to the net surface heat flux seen in reanalysis [e.g., cf. Fig. 1 with Kållberg et al. (2005, p. 12)]. The addition of $Q$ fluxes helps to produce a climatology resembling that of Earth. For simplicity, the aquaplanets' $Q$ fluxes are set to zero everywhere.

## 3. Regime characteristics

Monsoon onset is associated with sudden arrival of intense rainfall. Figure 2 shows the evolution of the

TABLE 1. Summary of experiments.

| Name | Ocean depth (m) | Land depth (m) | Topography | $Q$ fluxes |
|---|---|---|---|---|
| ap2 | 2 | — | — | Zero everywhere |
| ap10 | 10 | — | — | Zero everywhere |
| ap20 | 20 | — | — | Zero everywhere |
| ap20q | 20 | — | — | AMIP derived |
| am20 | 20 | — | Yes | AMIP derived |
| flat | 20 | 2 | — | AMIP derived |
| full | 20 | 2 | Yes | AMIP derived |

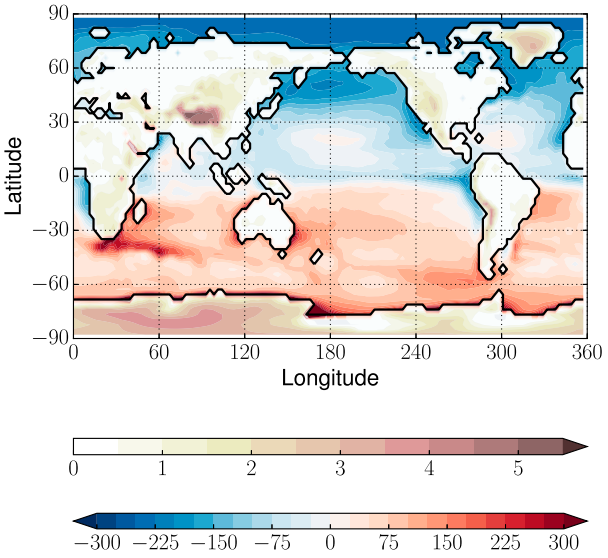


FIG. 1. Configuration of land and topography used in the full experiment. Color shading over land shows surface height; interval is 500 m. Color shading over ocean shows the average $Q$ flux in JJA; interval is 25 W m$^{-2}$. In both cases, white shading corresponds to zero.

modeled precipitation as a function of latitude and time for each of our simulations. A zonal average is shown for the aquaplanets. For the full experiment, an average between 60° and 150°E is used, which we take to be representative of the South and East Asian monsoon regions. In the full experiment, the peak precipitation shifts into the Northern Hemisphere in May and strengthens, before weakening and returning southward in September. The general structure of the precipitation climatology of the simulated Asian monsoon is consistent with that in observations from GPCP (see Fig. A1), indicating that, in the more realistic configuration, the model successfully captures the timing and behavior of the system.

Comparing the full experiment with the aquaplanets allows zonally symmetric and asymmetric processes to be distinguished. Some similarities are apparent. In the ap2 experiment, precipitation shifts quickly from one hemisphere to the other, spending little time centered on the equator, builds to a peak shortly after onset, then weakens and moves equatorward. The strong precipitation and the sharp transition of the ITCZ from Southern to Northern Hemisphere show that zonal asymmetries in the boundary condition are not essential for monsoon-like behavior. However, from the differences in latitudinal structure, and from the earlier and more gradual monsoon onset in the full experiment, it is clear that zonally asymmetric features play a role in determining the precipitation structure and advancing onset timing in the more realistic experiment. This is discussed further in section 6. We also note that rainfall is more intense in ap2 than the full experiment, and is associated with larger shifts of the ITCZ from the equator. These differences in displacement and magnitude are likely due to the fact that the average MLD of the full experiment is higher than in ap2, and that evaporation is limited over the continent in the full experiment. The effect of a deeper MLD can be seen in the ap20 experiment, where peak precipitation undergoes much smaller excursions from the equator. The deep MLD and lack of $Q$ fluxes in this experiment means that the surface temperature lags the peak insolation by about 90 days. This simulation does not exhibit other features of monsoon onset, with no reversal of the zonal wind direction (not shown). This experiment is presented as an example of a climate that remains in the equinoctial regime and for comparison with the other 20-m MLD ocean experiments (see Table 1).

Moist static energy (MSE) is also shown in Fig. 2, defined as

$$\mathrm{MSE} = c_p T + Lq + gz, \tag{3}$$

where $c_p$ is the specific heat capacity of dry air at constant pressure, $T$ is temperature, $L$ is the latent heat of vaporization of water, $q$ is specific humidity, $g$ is the gravitational constant, and $z$ is height. In all simulations the strongest precipitation lies close to and slightly equatorward of the peak MSE, which in the ap2 experiment is collocated with the northward boundary of the winter Hadley cell (Fig. 3), consistent with Privé and Plumb (2007a).

To allow behavior before and after monsoon onset to be compared, 20-day periods, prior to and post onset, have been selected for the full and ap2 experiments. For each latitude and longitude over the monsoon region, the first 5-day period (pentad) at which precipitation exceeds 8 mm day$^{-1}$ was identified. This was used as an indicator of the arrival of the monsoon. Maps of this onset date (not shown) were then used to identify pentad ranges before and after the monsoon rains develop over South and East Asia, or over the equivalent latitudes for the ap2 experiment. For both full and ap2

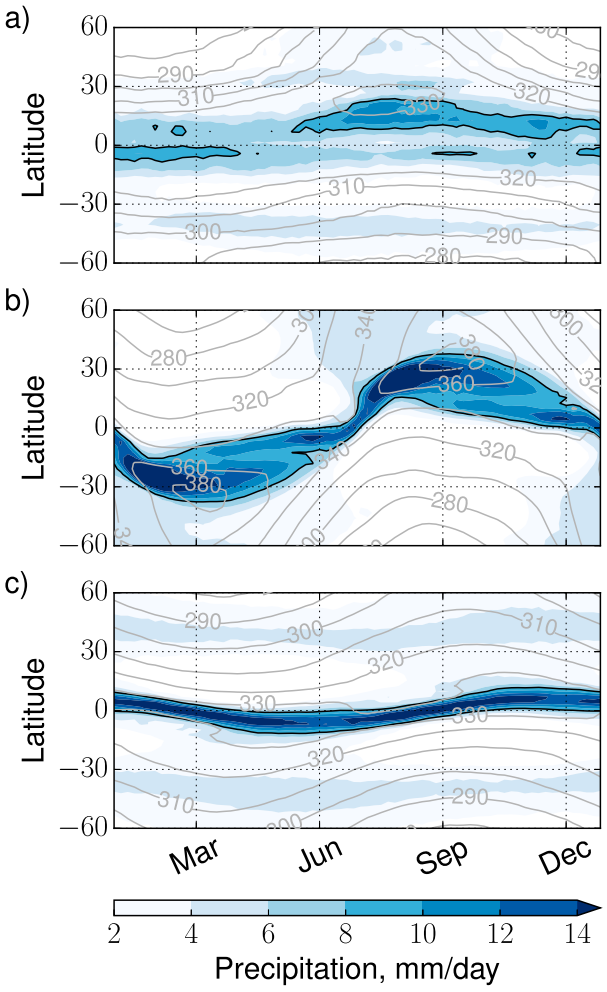


FIG. 2. Seasonal cycle of zonal mean precipitation (mm day$^{-1}$; color shading) for the (a) full, (b) ap2, and (c) ap20 experiments. Averages are over all longitudes for the aquaplanet experiments and between 60° and 150°E for the full experiment. The 8 mm day$^{-1}$ contour is marked in black. Gray contours indicate MSE at 850 hPa (kJ kg$^{-1}$).

experiments, the monsoon is well established by mid-July, and a 20-day period between 16 July and 5 August was selected (note the use of 30-day months in the experiments). Preonset periods were selected as 1–20 June for ap2 and 1–20 April for the full experiment.

Before monsoon onset, in both the ap2 and full simulations, two overturning cells are seen, roughly centered around the equator (Fig. 3). Strong westerly zonal jets are found in both hemispheres. After onset, the circulation strength of the Southern Hemisphere Hadley cell increases significantly, and the cell extends across the equator. Upper-level easterlies develop, and the Northern Hemisphere cell shifts poleward and weakens. As with the precipitation, differences again arise from the land, topography, and $Q$ flux distribution in the full experiment. Here, after onset, two components to the overturning cell are seen. Warm surface temperatures over the coastline and Indian Ocean, and orographic forcing by the Tibetan Plateau, result in a first region of low level ascent at around 10°N. A second counterclockwise overturning cell forms to the north of this, with air descending on the poleward side of the Tibetan Plateau and warming at lower levels. Section 6 discusses the roles of the different aspects of the surface boundary condition in further detail.

Figures 2 and 3 suggest some relationship between the strength of the meridional overturning circulation $\Psi$ (and its associated precipitation), and the displacement of the ITCZ from the equator. The strongest precipitation occurs when the ITCZ is farthest north. Figure 4 shows the peak strength of the meridional overturning circulation associated with the winter cell $\Psi_{max}$ versus the latitude $\phi_0$, at which $\Psi$ drops below $120 \times 10^9$ kg s$^{-1}$, both at 500 hPa. The latter is taken as indicative of the northward extent of the winter cell and will be referred to as the ITCZ latitude. A nonzero threshold was chosen to isolate the southern component of the double overturning circulation over the Asian monsoon region in the full experiment, seen in Fig. 3. We justify using the boundary of the southern component of the overturning based on the fact that the peak MSE in the full experiment is located at around 20°N, close to the boundary of this cell (Fig. 2). As stated above, peak MSE in an aquaplanet is known to be collocated with the northward boundary of the winter Hadley cell (Privé and Plumb 2007a). Each point in Fig. 4 corresponds to a multiyear pentad mean, so that the points closest to the equator correspond to the equinoctial season, while those farthest from the equator correspond to Northern Hemisphere summer. To find the ITCZ latitude, the meridional overturning was interpolated onto a 0.1° latitude axis and the first latitude at which the overturning strength passes the threshold was identified. The values plotted are for the onset phase of the monsoon, taken as the period of time during which the ITCZ is migrating northward and the overturning strength is increasing. We note that the peak strengths in Fig. 4 are stronger than those found in reanalysis (e.g., Kållberg et al. 2005). Note that 20-day multiyear means (Fig. 3) appear to be of more comparable magnitude to the reanalysis, suggesting that these large values are due to the shorter 5-day multiyear mean used for Fig. 4.

Figure 4 confirms that there is a positive relationship between overturning strength and latitude. Looking first at the aquaplanet experiments (black), the data suggest a change in the relationship between $\phi_0$ and $\Psi_{max}$ as the winter cell extends past about 7°N. Data from the ap20 (plus signs) and ap2 (black crosses) experiments are scattered at lower and higher latitudes

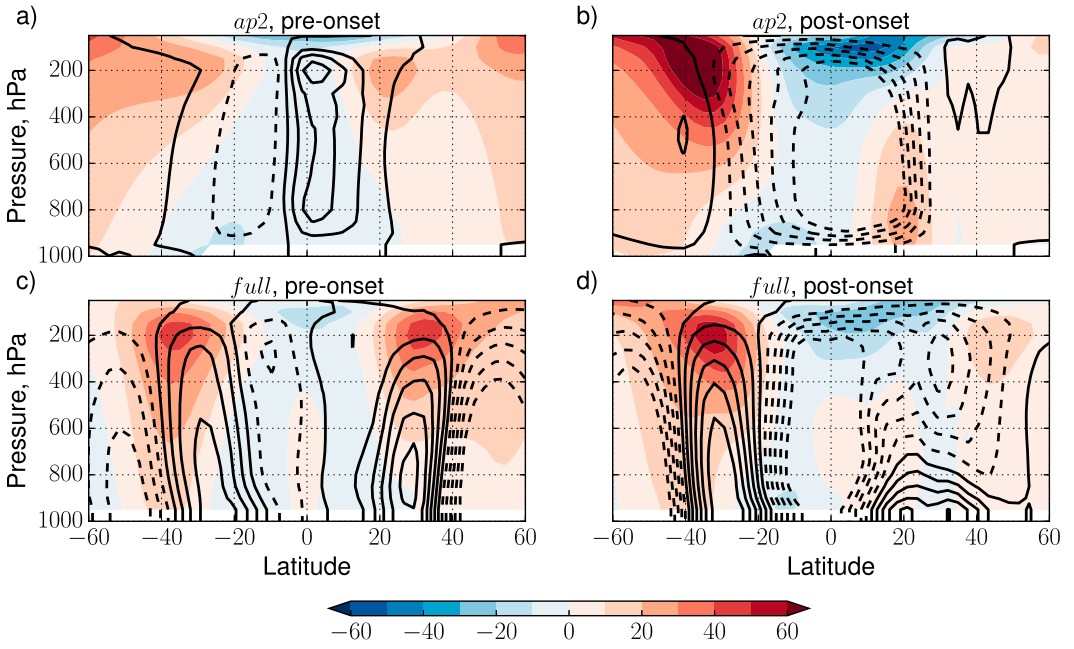


FIG. 3. Mass streamfunction $\Psi$ (black contours) and zonal wind ($\mathrm{m\,s^{-1}}$; color shading) for the (a),(b) ap2 and (c),(d) full experiments. Quantities are zonal and time averages over (a),(c) 20 days prior to monsoon onset and (b),(d) 20 days after monsoon onset. In (a) and (b) the zonal mean is taken over all longitudes; in (c) and (d) it is between 60° and 150°E. Onset is defined as arrival of precipitation above 8 mm $\mathrm{day^{-1}}$ (cf. Fig. 2). Contour interval is $60 \times 10^9\,\mathrm{kg\,s^{-1}}$ for $\Psi$. Solid contours indicate zero and positive values, and dashed contours are negative values.

respectively, and appear to show an increase in gradient of the scatter as ITCZ latitude increases, consistent with the proposed dynamical regime change during onset. As there is little overlap in scatter between these two experiments, a third aquaplanet with an MLD of 10 m (black dots) is also plotted, which spans both the low and higher latitudes, and confirms this behavior. The scatter is roughly consistent between the three experiments. For the full experiment (red crosses), data are averaged over the monsoon region. A gradient change is also seen in this experiment, although it is less pronounced. At higher latitudes the data points fit tightly around a straight line. At lower latitudes the scatter is broader, but appears to follow a shallower gradient, particularly south of 5°N. Qualitatively this gradient change behavior is similar to the simpler aquaplanet experiments.

The dashed lines in Fig. 4 show least squares best fits between the natural logarithms of both quantities for the ap10 (black) and full experiments (red). For the purposes of fitting, the data are divided into ITCZ latitudes north and south of 7°N (this choice of latitude is justified in the following section). The result is two power laws. For the ap10 experiment, at lower latitudes a relation $\Psi_{\max} = (276 \pm 7)\phi_0^{0.09\pm0.02}$ is obtained, while at higher latitudes the data follow $\Psi_{\max} = (121 \pm 48)\phi_0^{0.49\pm0.16}$. The uncertainties quoted correspond to two standard errors on the log–log scale. From the full experiment, the relationships $\Psi_{\max} = (151 \pm 32)\phi_0^{0.27\pm0.15}$ and $\Psi_{\max} = (108 \pm 24)\phi_0^{0.45\pm0.09}$ are found. The Student's $t$ test confirms that the lower- and higher-latitude fits are significantly different at a 95% confidence level in both cases. The higher-latitude power law is similar to that for the ap10 experiment, and in particular the exponent obtained for higher-latitude ITCZs is strikingly close in value to that for the aquaplanet. The lower-latitude power laws are less similar but are still suggestive of regime change behavior in the more realistic simulation. Schneider and Bordoni (2008) investigated similar behavior in dry, steady-state aquaplanet simulations in which the latitude of peak thermal forcing was varied. They identified exponents of 1/5 and 4/3. These are larger than the values obtained in our aquaplanet experiments, possibly reflecting that the seasonal cycle means that our simulations do not reach an equilibrium state, or that the presence of moisture affects the relationship.

Varying the choice of model level, or threshold for the ITCZ latitude, confirms that the qualitative behavior is not dependent on these, but the precise relation obtained does vary. For ITCZ thresholds between 90 and $150 \times 10^9\,\mathrm{kg\,s^{-1}}$ and model levels between 400 and 850 hPa, ap10 (full) experiment values between 0.05 and 0.14 (between 0.19 and 0.34) are obtained for the exponent in the lower-latitude relation, while values between 0.23 and 0.65 (between 0.29 and 0.91) are obtained for

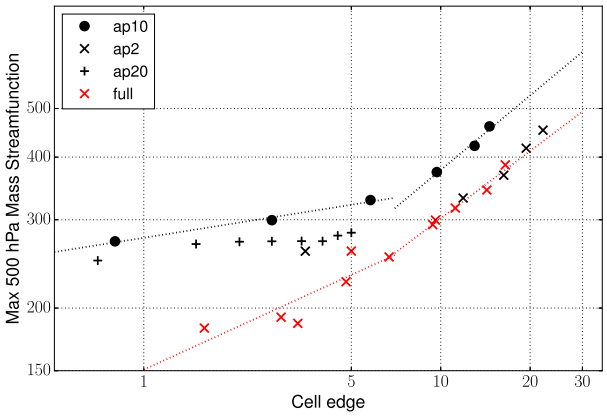


FIG. 4. Peak strength of the meridional overturning associated with the cross-equatorial Hadley cell vs latitude of the ascending branch, both at 500 hPa and during monsoon onset in the Northern Hemisphere. Each point corresponds to a 5-day mean. For the full experiment, points are a zonal average between 60° and 150°E. The black and red dotted lines indicate best-fit power laws for the ap10 and full experiments, respectively. Latitudes south and north of 7°N cell edge are fitted separately.

higher latitudes. In all cases a higher exponent is found for the higher-latitude regime than for the lower. The exponents are generally significantly different in most cases for both experiments, exceptions being where only two data points are fitted in some aquaplanet cases so that the error on the slope is undefined, and when the fit is calculated at 400 hPa or with a threshold of $150 \times 10^9\,\mathrm{kg\,s^{-1}}$ for the full experiment. The similar behavior observed in the aquaplanet and more realistic experiments, particularly in the higher-latitude regime, suggests that the same dynamical processes are dominant over monsoon onset in both cases. The following sections will investigate the physics involved in more detail.

## 4. Vorticity budget

We have shown that once the ITCZ moves sufficiently far from the equator, the overturning circulation strengthens significantly in our model. We now investigate the dynamics responsible in more detail. There is a general agreement in the literature that the transition to the monsoon-like regime in aquaplanets is associated with a reduction in magnitude, or a reversal, of upper-level absolute vorticity, so that the overturning becomes closer to thermally direct (Plumb and Hou 1992; Bordoni and Schneider 2008; Shaw 2014; Zhai and Boos 2015). The difference in absolute vorticity at 150 hPa before and after monsoon onset in the full experiment (see Fig. 12d, discussed further in section 6) is roughly consistent with this. Absolute vorticity decreases in a band centered over the Tibetan Plateau, and increases in the Southern Hemisphere. The sign of these changes corresponds to a reduction in magnitude in both hemispheres. However, an increase in absolute vorticity magnitude is found to the south of the Tibetan Plateau, between 0° and 30°N.

The causes of these changes can be investigated using the vorticity budget:

$$\frac{\partial \zeta}{\partial t} = -\mathbf{u}\cdot\nabla(\zeta+f) - \omega\frac{\partial \zeta}{\partial p} - (\zeta+f)\nabla\cdot\mathbf{u} + \mathbf{k}\cdot\left(\frac{\partial \mathbf{u}}{\partial p}\times\nabla\omega\right), \tag{4}$$

where $\zeta$ is relative vorticity, $\mathbf{u}$ is the horizontal wind vector, and $\omega$ is the pressure velocity. From left to right, the terms on the right-hand side of the above equation correspond to horizontal advection of vorticity, vertical advection of vorticity, vortex stretching, and vortex tilting. At upper levels, we find that the terms in $\omega$ are negligible compared with the other tendencies. In this section, we present plots of a climatology at 150 hPa based on pentad means. Over these short averaging periods, relative vorticity is evolving, and so is not in steady state. Imbalances in the budget may therefore be interpreted as the driver of changes to the upper-level absolute vorticity.

To understand the physics of the regime change, we first discuss the behavior of the simpler ap2 experiment. Figure 5 shows the seasonal evolution of the multiyear pentad and zonal mean horizontal advection, vortex stretching, and transient eddy terms in Eq. (4). The tendencies themselves are shown in Figs. 5a,d,g. The remaining panels show a breakdown of the dominant components of these: $\partial(\overline{\zeta}+f)/\partial y$ and $\overline{v}$ for the horizontal advection term and $\nabla\cdot\overline{\mathbf{u}}$ and $\overline{\zeta}+f$ for the stretching term. Transient eddies are broken down into components associated with horizontal advection and vortex stretching; in this case the sum of these recovers the total. Also shown in Figs. 5a,d,g are contours of the mass streamfunction at 150 hPa, with the zero line shown in the darker shade, to provide context as to where the tendencies peak in relation to the overturning structure.

In the tropics and subtropics, the time means of the zonal mean terms are dominant over transient eddies. When the ITCZ crosses the equator, both zonal mean tendencies change sign. In Northern Hemisphere summer, the tendency from horizontal advection is positive, and strongest close to the equator. Southward mean flow in the upper branch of the cross-equatorial cell advects higher absolute vorticity air downgradient. Horizontal advection therefore acts to increase the magnitude of absolute vorticity in the Northern Hemisphere, and to reduce the magnitude in the

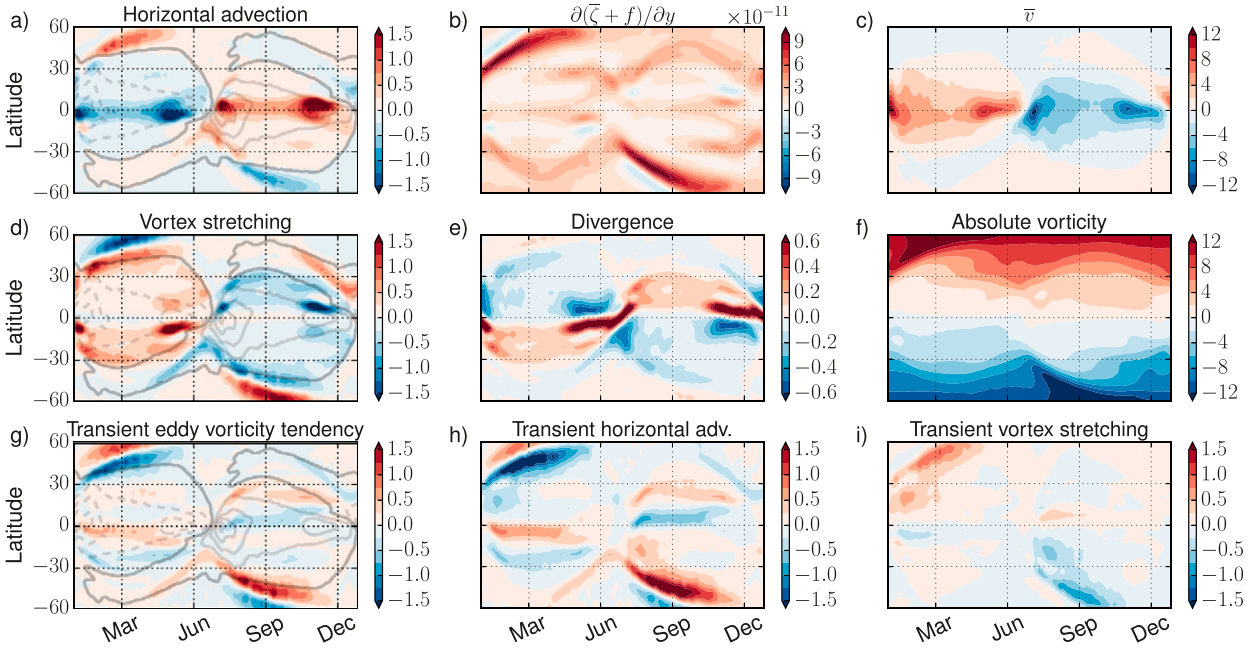


FIG. 5. Seasonal cycle and breakdown of terms in the vorticity budget from Eq. (4) for the ap2 simulation at 150 hPa, as a multiyear pentad mean, averaged over all longitudes: (a) $-\overline{\mathbf{u}}\cdot\nabla(\overline{\zeta}+f)$ (day$^{-2}$), (b) $\partial(\overline{\zeta}+f)/\partial y$ (m$^{-1}$ s$^{-1}$), (c) $\overline{v}$ (m s$^{-1}$), (d) $-(\overline{\zeta}+f)\nabla\cdot\overline{\mathbf{u}}$ (day$^{-2}$), (e) $\nabla\cdot\overline{\mathbf{u}}$ (day$^{-1}$), (f) $\overline{\zeta}+f$ (day$^{-1}$), (g) $-\nabla\cdot\overline{\zeta'\mathbf{u}'}$(day$^{-2}$), (h) $-\overline{\mathbf{u}'}\cdot\nabla\overline{\zeta'}$(day$^{-2}$), and (i) $-\overline{\zeta'\nabla\cdot\mathbf{u}'}$(day$^{-2}$). Gray contours in (a),(d),(g) show the mass streamfunction at 150 hPa. The contour interval is $100\times10^9$ kg s$^{-1}$. The dark gray contour is the zero contour, and solid contours indicate negative values for clarity during Northern Hemisphere summer.

Southern Hemisphere. The tendency from vortex stretching is instead negative during Northern Hemisphere summer, because of divergent flow over regions of ascent in the Hadley and Ferrel cells. Vortex stretching associated with ascent in the ITCZ reduces the Northern Hemisphere absolute vorticity. The combined effect of the two tendencies is to produce and reinforce a latitudinally broad region of reduced magnitude absolute vorticity air (Fig. 5f).

Looking more closely at the structure of the advective and stretching vorticity tendencies, it can be seen that monsoon onset and withdrawal are marked by peaks in both terms. We propose that these peaks connect to the regime change seen in Fig. 4. Breaking down the terms into components reveals a possible explanation for this sudden change. Figures 5e and 5f show the divergence and absolute vorticity, respectively, which multiply to give the stretching term. Absolute vorticity is near zero close to the equator, where planetary vorticity is small. Divergence, however, is strongest while the ITCZ is close to the equator, where it is narrow (see, e.g., Fig. 2). As the ITCZ shifts poleward, it moves into a region with nonnegligible absolute vorticity. The vortex stretching tendency increases significantly as the ITCZ migrates, with the peak during onset located nearest to the latitude grid point at 6.9°N. This tendency acts to reduce the local absolute vorticity, allowing a more thermally direct circulation to develop. This strengthens the overturning, as seen in Fig. 4. The region of ascent expands as the ITCZ moves poleward, so that the divergence is weaker and occupies a larger area. However, the vortex stretching tendency is still sufficient to lower absolute vorticity over a broad area, further strengthening the circulation.

The peak in the stretching term provides a physical justification for the 7°N threshold used for the fitting in Fig. 4. Once ascent moves sufficiently far from the equator that absolute vorticity is not negligible, the vortex stretching tendency increases. This lowers absolute vorticity over a larger region, triggering a change to a thermally direct circulation.

The peaks of the horizontal advection tendency also relate to the narrow near-equator ITCZ. The leading-order component of this is $\overline{v}\partial(\overline{\zeta}+f)/\partial y$. When the ITCZ is close to the equator, both the ascent and the associated upper-level divergent winds occur over a narrower area, resulting in strong meridional flow (Fig. 5c). At higher latitudes, $\overline{v}$ is negligible. The meridional gradient of absolute vorticity (Fig. 5b) peaks on the equator, decreases poleward, and peaks again in the midlatitudes. The combination of these terms yields strong horizontal

advection close to the equator during monsoon onset and withdrawal.

The contribution from eddies increases slightly in the summer hemisphere, but lags the sign change and increase of the other two terms, and is comparatively lower in magnitude, suggesting this is a response to instability of the circulation in the monsoon regime. Eddies play a dominant role in balancing the vortex stretching and horizontal advection around the descending parts of the winter Hadley cell, and around the ascending and descending parts of the Ferrel cell. From the breakdown of the eddy term in Figs. 5h,i, it can be seen that eddies associated with horizontal advection of vorticity account for the majority of eddy activity observed.

The roles of the horizontal wind speed, the absolute vorticity, and their gradients in determining the sign and magnitude of the vorticity tendencies in the equinoctial regime and over onset are summarized in Fig. 6. Over most of the year, with the exception of monsoon onset, the model climate evolves slowly (e.g., the residual of the zonal momentum budget is near zero; see Fig. 8f). Monsoon onset appears to correspond to a fast transition between climates close to the two steady-state solutions to Eq. (1), driven by the feedbacks described above. While the present paper discusses the processes involved over monsoon onset in a time-varying case, the steady-state budget will be explored further in future work.

The key features of the vorticity budget for the ap2 experiment are shared with the full experiment (Fig. 7). The reduction in absolute vorticity magnitude during monsoon onset is less marked in the full experiment than in ap2, but a broadening of the low-magnitude region is still observed in Northern Hemisphere summer. Horizontal vorticity advection and vortex stretching are again the dominant terms in the budget, and act to reduce the magnitude of the Southern and Northern Hemisphere absolute vorticity respectively. As in the ap2 experiment, transient eddies are weak, except at the edge of the Southern Hemisphere cell during winter. Differences from the ap2 experiment can, however, be seen, which relate to the structure of the land and topography. During Northern Hemisphere summer, both terms now have multiple peaks in latitude. Looking first at the stretching term, peaks are found corresponding to the ascending regions seen in Fig. 3. At around 20°N, ascent is forced by the Tibetan Plateau, and by warm sea surface temperatures along the coastline. This is balanced by horizontal advection over the upper branch of the Hadley cell, resulting in the region of increased absolute vorticity visible in Fig. 7f. Air descends to the north of the plateau and ascends again between 30° and 40°N, particularly over the eastern side of the continent (see Fig. 12, discussed in section 6). The vortex stretching associated with this ascending region dominates over horizontal advection, so that a latitudinally broad region of low absolute vorticity air is still realized, extending across the continent. From the breakdown of the stretching term (Figs. 7e,f), similar behavior to the ap2 experiment is found. Divergence is strong along the equator, but, as absolute vorticity is small here, vortex stretching is weak. Once ascent is forced farther to the north, vortex stretching strengthens and acts to lower absolute vorticity.

In both Figs. 5 and 7, we have identified a sharp increase in the vorticity tendency resulting from vortex stretching during monsoon onset. This occurs once the ITCZ reaches latitudes where absolute vorticity is no longer negligible. Vortex stretching and cross-equatorial advection of vorticity then create a broad region of low, although nonzero, absolute vorticity (see Fig. 6). In the ap2 experiment it is the warming of the surface by the seasonally varying insolation that results in off-equatorial ascent, whereas in the full experiment localized warming of the ocean and forcing by the Tibetan Plateau also play a role (discussed further in section 6). Regardless of the driving mechanism, once the ITCZ shifts sufficiently far from the equator, vortex stretching and advection by the meridional overturning flow result in a quick intensification of the cross-equatorial Hadley cell.

## 5. Role of zonal asymmetry

While we have found that vortex stretching in off-equatorial regions of ascent is key in the regime transition in both the ap2 and full experiments, differences in behavior between the experiments are evident from the vorticity budgets. The processes responsible for triggering the transition in the more realistic experiment will now be investigated in further detail. In particular, we would like to distinguish the roles in the full experiment of zonally symmetric warming of a low thermal inertia surface, the key process in the ap2 experiment, and land–sea contrast and orographic forcing. In the derivation of the vorticity budget, pressure gradient terms cancel. We therefore evaluate the zonal momentum budget in order to assess the effect of these gradients, which we expect to be forced by zonal asymmetries in the surface conditions of the full experiment.

Separating nonlinear terms into a zonal-temporal mean state and transient and stationary eddies (e.g., Peixoto and Oort 1992, 61–65), the primitive equation for $u$ in pressure coordinates can be expressed as

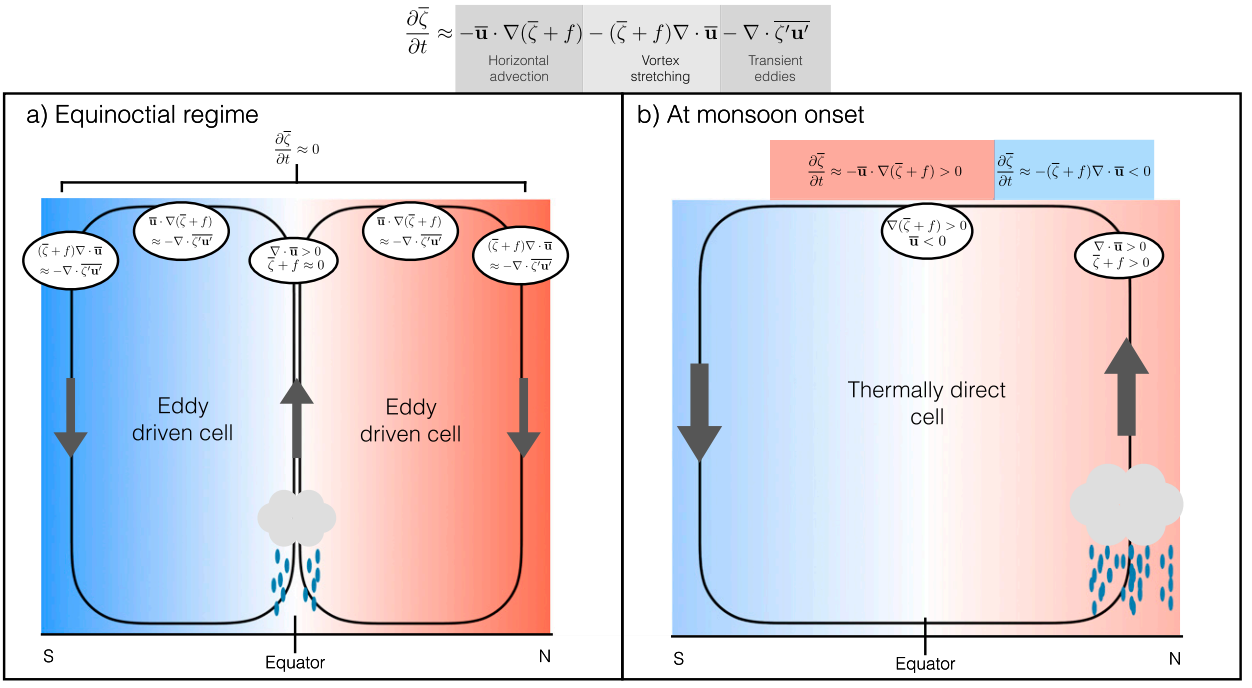


FIG. 6. Schematic summarizing the behavior in the equinoctial regime and over monsoon onset seen in the ap2 simulation. Shading indicates absolute vorticity, arrows indicate the direction and strength of the overturning circulation. (a) In the equinoctial regime, ascent occurs close to the equator where absolute vorticity is near zero. Off the equator, absolute vorticity and its gradient are nonnegligible, but the weak zonal mean tendencies are balanced by eddies. The total vorticity tendency is small, and the circulation is near to the "weak overturning" steady-state solution of Eq. (1). (b) At monsoon onset, ascent occurs off the equator where absolute vorticity is nonnegligible. This results in a negative upper-level vorticity tendency resulting from vortex stretching in the Northern Hemisphere, reducing the magnitude of the absolute vorticity. The circulation begins to transition to the thermally direct steady-state solution of Eq. (1), and the overturning strengthens. The cross-equatorial meridional flow is associated with a positive vorticity tendency resulting from horizontal advection, which reduces absolute vorticity magnitude in the Southern Hemisphere. The vorticity tendencies resulting from vortex stretching and horizontal advection therefore both act to further reduce the magnitude of absolute vorticity. This positive feedback allows overturning strength, and the associated precipitation, to increase rapidly over onset.

$$\frac{\partial\overline{u}}{\partial t} = f([\overline{v}]+\overline{v}^*) - \frac{\partial\overline{\Phi}^*}{\partial x} + \overline{\mathscr{F}^{(x)}} - \left([\overline{v}]\frac{\partial[\overline{u}]}{\partial y} + [\overline{\omega}]\frac{\partial[\overline{u}]}{\partial p}\right) - \left(\overline{u}^*\frac{\partial\overline{u}^*}{\partial x} + \overline{v}^*\frac{\partial\overline{u}^*}{\partial y} + \overline{\omega}^*\frac{\partial\overline{u}^*}{\partial p}\right)$$
$$- \left([\overline{u}]\frac{\partial\overline{u}^*}{\partial x} + [\overline{v}]\frac{\partial\overline{u}^*}{\partial y} + [\overline{\omega}]\frac{\partial\overline{u}^*}{\partial p}\right) - \left(\overline{v}^*\frac{\partial[\overline{u}]}{\partial y} + \overline{\omega}^*\frac{\partial[\overline{u}]}{\partial p}\right) - \left(\frac{\partial\overline{u'u'}}{\partial x} + \frac{\partial\overline{u'v'}}{\partial y} + \frac{\partial\overline{u'\omega'}}{\partial p}\right), \quad (5)$$

where $u$, $v$, and $\omega$ are the zonal, meridional, and vertical winds in pressure coordinates, respectively; $\mathscr{F}^{(x)}$ describes frictional damping; and $\Phi$ represents geopotential. As in Eq. (1), overbars indicate the multiyear pentad mean, and primes denote a deviation from this. We again note that, over the short 5-day averaging periods considered, the climate is not in steady state, so that $\partial\overline{u}/\partial t$ is not necessarily zero, though it is generally a small residual. Square brackets and asterisks similarly represent the zonal mean over all longitudes and stationary eddies, respectively, so that, for example, $f\overline{v} = f[\overline{v}] + f\overline{v}^*$. The first three terms on the right-hand side correspond to acceleration of the temporal mean zonal wind via Coriolis force, geopotential gradients, and friction. The following terms in parentheses represent advection of zonal momentum by the zonal mean flow (first), stationary eddies (second, third, and fourth), and transient eddies (fifth). Note that if the zonal mean of both sides is taken over all longitudes, the stationary eddy cross terms in the third and fourth terms in parentheses and the stationary eddy geopotential gradient term average to zero. This choice of decomposition is used to allow comparison with results of previous studies (e.g., Shaw 2014).

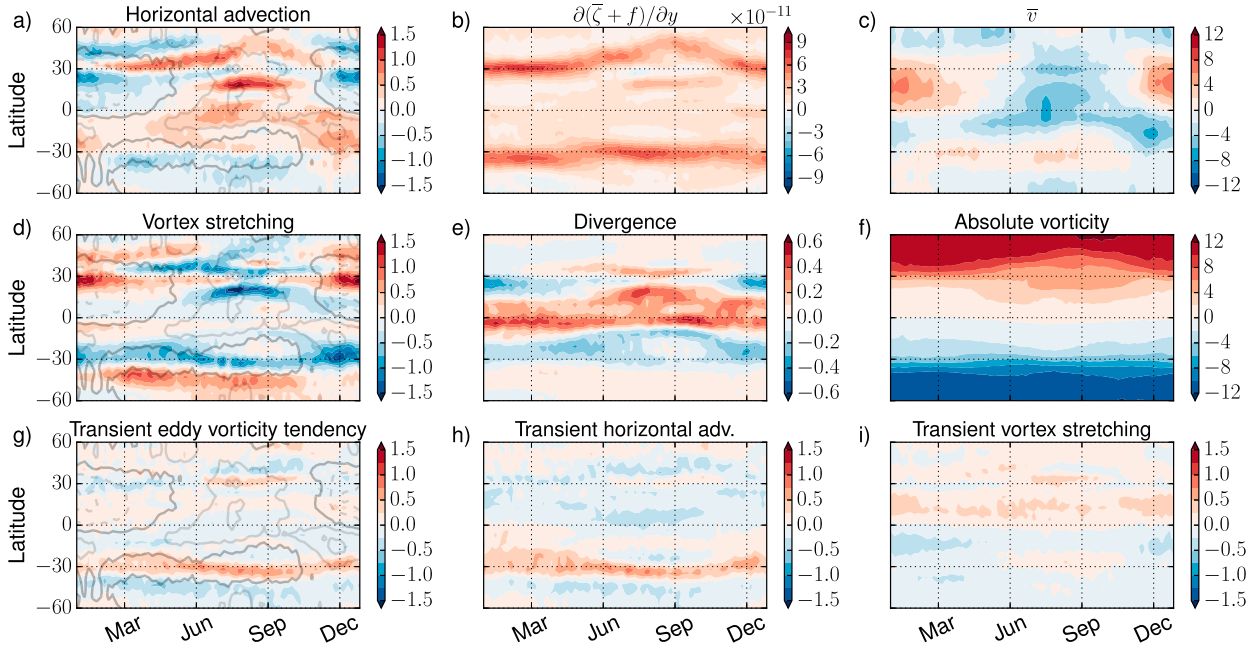


FIG. 7. As in Fig. 5, but for the full experiment, with zonal means defined between 60° and 150°E.

To identify the response when boundary conditions are zonally symmetric, we again look first at the ap2 experiment. The terms in the zonal momentum budget are plotted as a function of latitude and time in Fig. 8. A zonal average of Eq. (5) has been taken over all longitudes. The advective terms are shown as sums of the contributions associated with the mean state, transient and stationary eddies. Geopotential gradient and the total zonal wind tendency are included for completeness. The former is zero for a zonal average around a latitude circle, as it is a zonal gradient. The contribution from stationary eddies is also negligible, as this experiment has zonally symmetric boundary conditions.

In late June, a fast change in the sign of $f[\overline{v}]$ (Fig. 8a) can be seen, reflecting the change in the direction of the upper-level meridional wind from northward to southward flow. This occurs as the ITCZ shifts into the Northern Hemisphere, bringing intense precipitation. The transition is associated with a change in sign, and an increase in magnitude, of the advection of momentum by the zonal and temporal mean state (Fig. 8b). This term is dominated by the meridional component $[\overline{v}]\partial[\overline{u}]/\partial y$. The balance of Coriolis acceleration and advection is consistent with low zonal mean absolute vorticity throughout the tropics and subtropics, as was discussed above.

While the boundary conditions in the ap2 experiment are symmetric, transient eddies (Fig. 8d) still play a role in the momentum budget. As the monsoon arrives, the transient eddy activity associated with the midlatitude storm track shifts poleward in the winter hemisphere, and weakens in the summer hemisphere. As with the vorticity budget, a weak increase in low-latitude eddy momentum flux convergence is also seen in the summer hemisphere after the shift in the precipitation band. This low-latitude eddy momentum flux convergence lags monsoon onset and damps the upper-level easterlies (see Fig. 3), suggesting it relates to instability associated with the easterly jet. However, this term is small compared with the mean flow, suggesting that the cell is predominantly thermally direct, particularly compared with the equinox period prior to monsoon onset, where the eddy and mean state terms are both small and of similar magnitude.

The equivalent budget for the full experiment is shown in Fig. 9. An average of Eq. (5) is here taken over the monsoon region used previously (60°–150°E), so that the local balance of eddy terms, the Coriolis force, and the geopotential gradient can be seen in addition to the zonal mean budget. In this experiment, the zonal mean Coriolis force associated with the cross-equatorial Hadley cell is not dominantly balanced by mean state advection, but instead by stationary eddy flux convergence. This is consistent with the results from reanalysis (Shaw 2014). A sense of how the localized features of the circulation arise can be gained from the stationary eddy Coriolis force, geopotential gradient, and cross terms in the monsoon region (Figs. 9f–h). It can be seen that the increase in cross-equatorial flow is significantly stronger here than in the zonal mean (stationary eddy

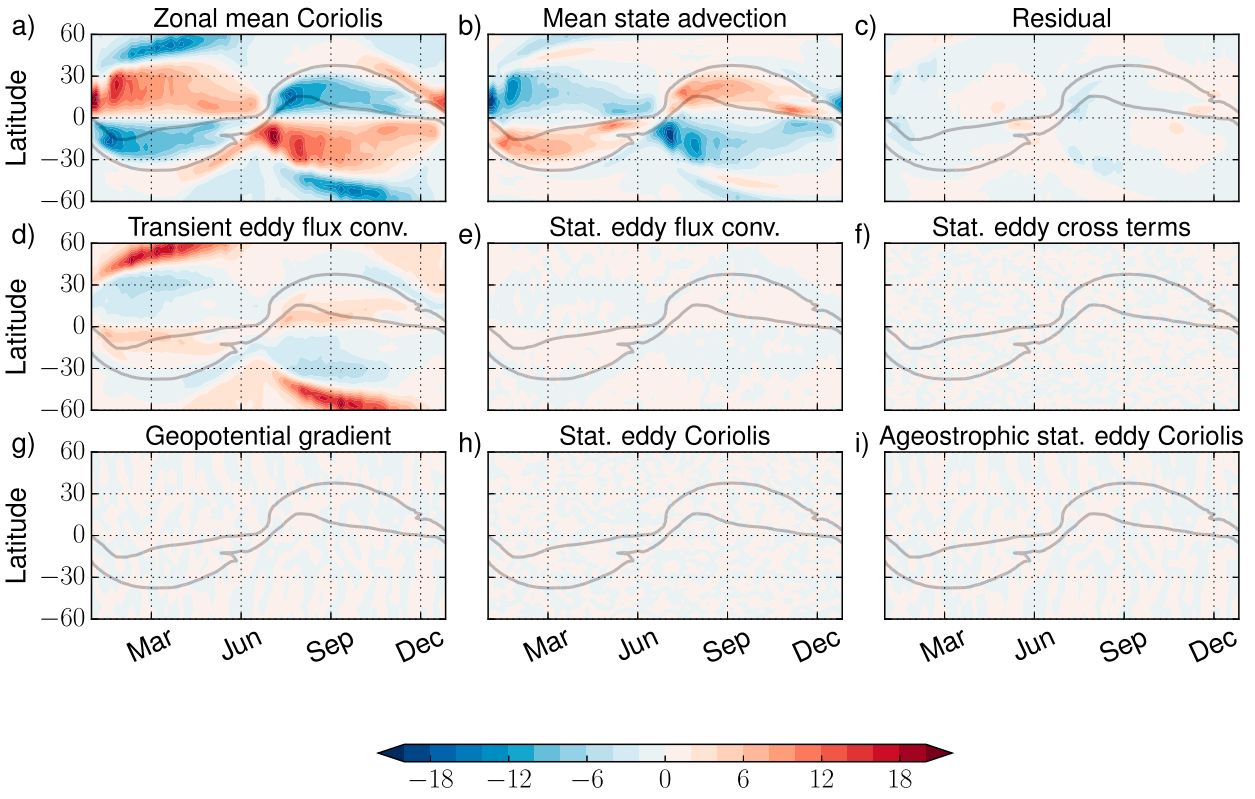


FIG. 8. Seasonal cycle of the terms in the zonal momentum budget ($\mathrm{m\,s^{-1}\,day^{-1}}$) from Eq. (5) for the ap2 simulation at 150 hPa: (a) $f[\overline{v}]$, (b) $-([\overline{v}]\partial[\overline{u}]/\partial y + [\overline{\omega}]\partial[\overline{u}]/\partial p)$, (c) $\partial\overline{u}/\partial t$, (d) $-(\partial\overline{u'u'}/\partial x + \partial\overline{u'v'}/\partial y + \partial\overline{u'\omega'}/\partial p)$, (e) $-(\overline{u}^*\partial\overline{u}^*/\partial x + \overline{v}^*\partial\overline{u}^*/\partial y + \overline{\omega}^*\partial\overline{u}^*/\partial p)$, (f) $-(\overline{v}^*\partial[\overline{u}]/\partial y + \overline{\omega}^*\partial[\overline{u}]/\partial p) - ([\overline{u}]\partial\overline{u}^*/\partial x + [\overline{v}]\partial\overline{u}^*/\partial y + [\overline{\omega}]\partial\overline{u}^*/\partial p)$, (g) $-\partial\overline{\Phi}^*/\partial x$, (h) $f\overline{v}^*$, and (i) $(f\overline{v}^* - \partial\overline{\Phi}^*/\partial x)$. All quantities are multiyear pentad and zonal averages over all longitudes. The 8 mm $\mathrm{day^{-1}}$ precipitation contour is shown in gray in all panels as an indicator of monsoon onset.

Coriolis; Fig. 9h). At first glance, this appears dominantly in balance with the geopotential gradient (Fig. 9g), suggesting it is connected to pressure gradients driven by the orography and surface temperature distribution. To separate the geostrophic and ageostrophic components of the flow, we additionally show the ageostrophic stationary eddy Coriolis force ($fv_a^* = f\overline{v}^* - \partial\overline{\Phi}^*/\partial x$) in Fig. 9i. It can be seen that $fv_a^*$ also shows an increase in magnitude over monsoon onset, and is again much stronger than the zonal mean Coriolis force. South of about 20°N, the geopotential gradient does not balance the stationary eddy Coriolis force, and the dominant balance is instead between $fv_a^*$ and advection by stationary eddy cross terms (Fig. 9f). North of this, geostrophic balance dominates, but a nonnegligible ageostrophic component is still present.

The intensification of the ageostrophic stationary eddy Coriolis force shows that the flow is locally stronger than that driven by the geopotential gradient, making it clear that there is more than just land–sea contrast involved, and that some additional strengthening of the overturning takes place via dynamical interactions. From this perspective, the balance of the ageostrophic stationary eddy Coriolis force and stationary eddy cross terms in the full experiment bears some similarity to the balance of the Coriolis force and mean state advection in the ap2 experiment. However, there are important differences between these cases. First, whereas in the ap2 experiment the Coriolis force and mean state advection exhibit rapid enhancement and changes of sign, in the full experiment $fv_a^*$ does not change sign, and increases only once the geopotential gradient has strengthened. Second, whereas in the ap2 experiment the zonal mean state advection term is nonlinear in the mean state, the stationary eddy cross terms in the full experiment are linear in both the mean state and stationary eddy components of the flow. This is consistent with the success of linear models in simulating monsoon onset (e.g., Wang and Ting 1999).

Subtropical planetary-scale waves have been demonstrated to trigger a monsoon-like regime transition in an aquaplanet simulation with SST anomalies (Shaw 2014). The momentum budget analysis allows us to connect this

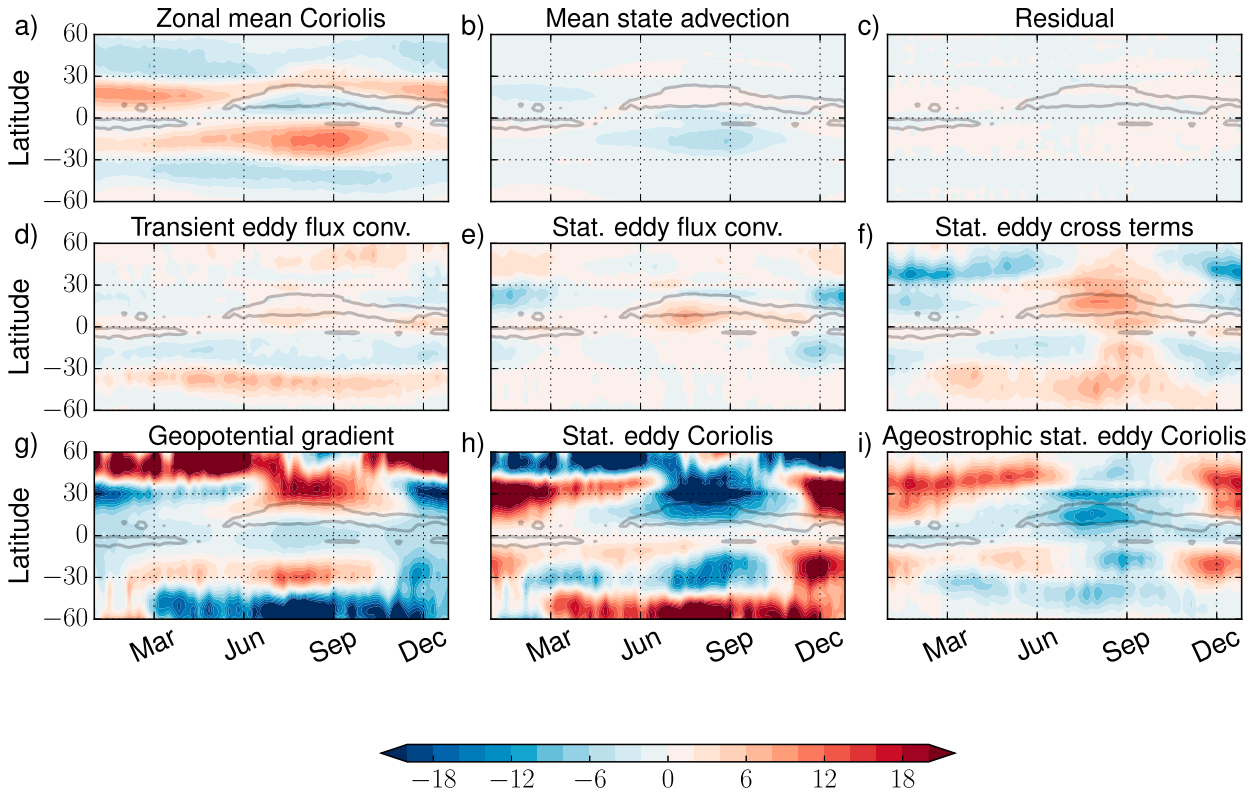


FIG. 9. As in Fig. 8, but for the full experiment, with the zonal average taken between 60° and 150°E. The 8 mm day$^{-1}$ precipitation contour averaged over this region is marked on all plots in gray as an indicator of monsoon onset.

to zonally symmetric theories for the monsoon regime change. Figure 10 shows the geopotential and horizontal streamfunction at 150 and 850 hPa after monsoon onset, and also the 850-hPa temperature for this period. The Asian and North American continents are warm relative to the ocean, and produce a wavenumber-2 signal in the lower level geopotential, centered on 30°N, with troughs over the land. This is mirrored by increased geopotential at upper levels. The streamfunction shows a cyclone over the Asian continent, in geostrophic balance with the geopotential. The South and East Asian monsoon regions lie in the area of this wave where the sign of the geopotential gradient is such as to extend the overturning circulation farther north, as seen in Fig. 3. South of 20°N, where geopotential gradient is weak and streamlines are roughly oriented east–west, the wave forces an intensified localized circulation.

The Asian monsoon is often considered to consist of two interacting systems, the South Asian and East Asian monsoons. The former is considered an essentially tropical system, whereas in the latter midlatitude dynamics are thought to play more of a role. The monsoon arrives first over Indo-China, then progresses westward over India (Wu and Wang 2000). The results presented here suggest that the East Asian component of the monsoon relates to the stationary wave that emerges as the Northern Hemisphere continents heat up. Geostrophic northward flow and ascent are forced over the continent, and vortex stretching acts to lower upper-level absolute vorticity. The broad region of low absolute vorticity then triggers a transition of the lower-latitude overturning circulation into the intensified cross-equatorial regime over South Asia.

## 6. Role of SSTs, land, and topography

The zonal momentum budget shows that zonal asymmetry is important in driving the transition in the more realistic full experiment. To investigate the roles of SSTs, land, and topography across the continent, we now present results from the three intermediate experiments described in Table 1. To allow the roles of these different features to be identified, latitude–longitude time averages over the pre- and postonset periods used for the full experiment in section 3 are presented here for a selection of fields. We note that, as our experiments use prescribed $Q$ fluxes, ocean–atmosphere feedbacks are not fully represented. Additionally, the SST that does

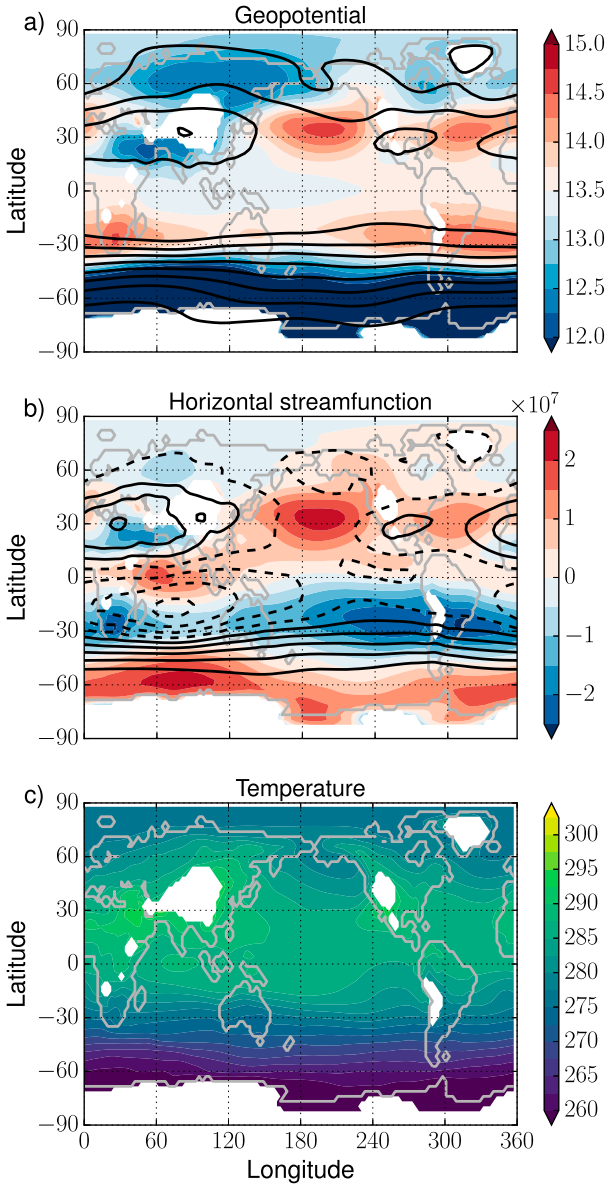


FIG. 10. (a) The 850- ($m^2 s^{-2}$color shading) and 150-hPa geopotential (contours; contour interval 2000 $m^2 s^{-2}$; peak over North America corresponds to 136 000 $m^2 s^{-2}$) for the full experiment. (b) Equivalent plots for the horizontal streamfunction at 850 ($m^2 s^{-1}$; color shading) and 150 hPa (contours; contour interval $2 \times 10^7 m^2 s^{-1}$). Dashed lines indicate negative values, and solid lines indicate the zero contour and positive values. (c) Temperature at 850 hPa (K). All plots are averaged over 20 days after monsoon onset. The land mask used is shown in gray. Missing values at 850 hPa are due to intersection with topography.

develop will be influenced by the atmospheric circulation. The $Q$ fluxes should therefore not be interpreted as an independent cause of differences in the circulation, although they do give an indication of the role of ocean heat transport and storage in monsoon onset.

Figure 11 shows the latitude–longitude precipitation distribution and 150-hPa horizontal wind vectors over the monsoon region for the experiments with nonzonally symmetric surface conditions. In the full experiment, precipitation is relatively weak prior to onset, particularly over the continent. A band of precipitation is seen around the equator and extending up the eastern coast of China over the ocean. Over onset, this coastal precipitation intensifies and migrates inland as the land warms. A region of strong precipitation develops around the Tibetan Plateau. The rain associated with the ITCZ shifts poleward, becoming particularly intense over India. The wind vectors show a change from strong westerlies over the continent and weak easterlies around the equator to an upper-level anticyclone centered on the Tibetan Plateau, associated with strong easterlies at low latitudes and a cross-equatorial flow.

From the intermediate experiments, the distribution of precipitation before onset appears fairly similar in all simulations. As $Q$ fluxes are the shared feature across all experiments, this indicates an important role for ocean heat transport. Comparing the full and am20 experiments with the ap20q and flat experiments, it can be seen that topography is needed to force precipitation over the continental region, where $Q$ fluxes are zero. After onset, rain is seen at low latitudes over India in all simulations, suggesting that warm SSTs are the most important factor in generating this part of the circulation. In the ap20q experiment, where there is no land to limit evaporation, precipitation exceeds 4 mm $day^{-1}$ over most of the continental region. At lower latitudes, precipitation is more intense when land or topography is included, particularly over Southeast Asia. The combination of both appears to be needed to force the distribution of precipitation seen in the full experiment. The wind distribution is also relatively similar in all experiments prior to onset, and after onset at low latitudes and in the Southern Hemisphere. The direction of curvature of the postonset wind over the continent is different without topography, indicating that this is important in generating the anticyclonic system. However, again both land and topography are needed to produce the wind distribution of the full experiment. It appears that the shallower land MLD strengthens the low pressure system that the topography forces over the continent.

Figure 12 shows the difference in absolute vorticity over monsoon onset for the intermediate experiments, and the average of the stretching and horizontal advection terms in the vorticity budget over monsoon onset. As was seen for the full experiment, over onset there is a decrease in absolute vorticity over the Asian continent. Interestingly this is again seen in the ap20q simulation, where there is no land or topography, and the only distinction from the permanently equinoctial

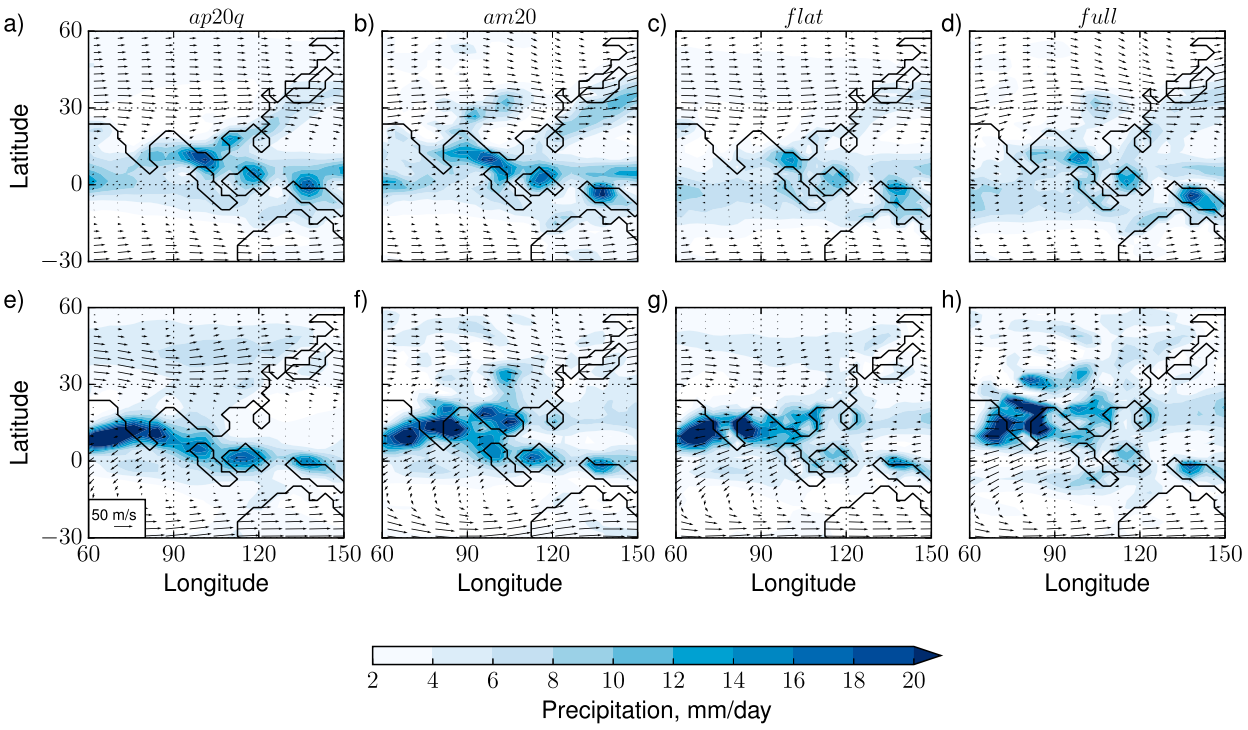


FIG. 11. Spatial distribution of precipitation and 150-hPa wind averaged over 20 days (a)–(d) before and (e)–(h) after monsoon onset. All experiments with nonzonally symmetric surface conditions are plotted. A reference vector for the 150-hPa wind is shown in (e).

ap20 simulation is $Q$ fluxes. This again emphasizes the importance of the evolution and asymmetry of SSTs in monsoon onset. However, the decrease in absolute vorticity in the intermediate simulations is smaller than that seen in the full experiment, and, as with the precipitation and winds, it is evident that the combination of land, topography, and $Q$ fluxes is needed to produce the behavior of the most realistic experiment. The am20 simulation comes closest to capturing the structure of the signal in the full experiment, with peaks to the north of the Tibetan Plateau and over the Pacific coast. This simulation also best captures the increase in absolute vorticity to the south of the Tibetan Plateau seen in the full experiment. Despite this area of increase, it can be seen for all experiments that the combination of strong vortex stretching and horizontal advection helps to create an extended region relatively low absolute vorticity air between 20°S and 30°N after monsoon onset (e.g., black contours are widely spaced at lower latitudes).

Figures 12e–l show the average of the vorticity tendencies from horizontal advection and vortex stretching over onset (between the periods shown in Fig. 11). As discussed in section 4, in the full experiment two regions of negative vortex stretching can be seen, one over India and Southeast Asia and one to the north of the Tibetan Plateau, across the continent and Pacific coastline, associated with ascent around the low pressure center over the continent. We note that the latitude–longitude distribution highlights that there is also upper-level convergence associated with this low pressure system, to the west and south of the Tibetan Plateau. This appears to explain the increase in absolute vorticity seen in this region in Fig. 12d, which is much weaker in the experiments without topography. In general, topography gives the strongest vorticity tendencies for both vortex stretching and horizontal advection, compared with the ap20q and flat experiments. However, these tendencies largely balance one another, so that the differences in absolute vorticity between the experiments (Figs. 12a–d) are less pronounced.

The 150-hPa zonal wind tendency resulting from the geopotential gradient [see Eq. (5)], shown in Fig. 13, makes the differences in stationary wave structure between the experiments clear. Before monsoon onset, the structure of geopotential gradient in the ap20q and flat experiments is relatively similar, indicating that the $Q$ fluxes are largely responsible in determining the geopotential distribution when there is no topography. The experiments including topography, am20 and full simulations, instead both have strong geopotential gradients over the continent, to the northeast of the Tibetan Plateau. After onset, however, significant differences

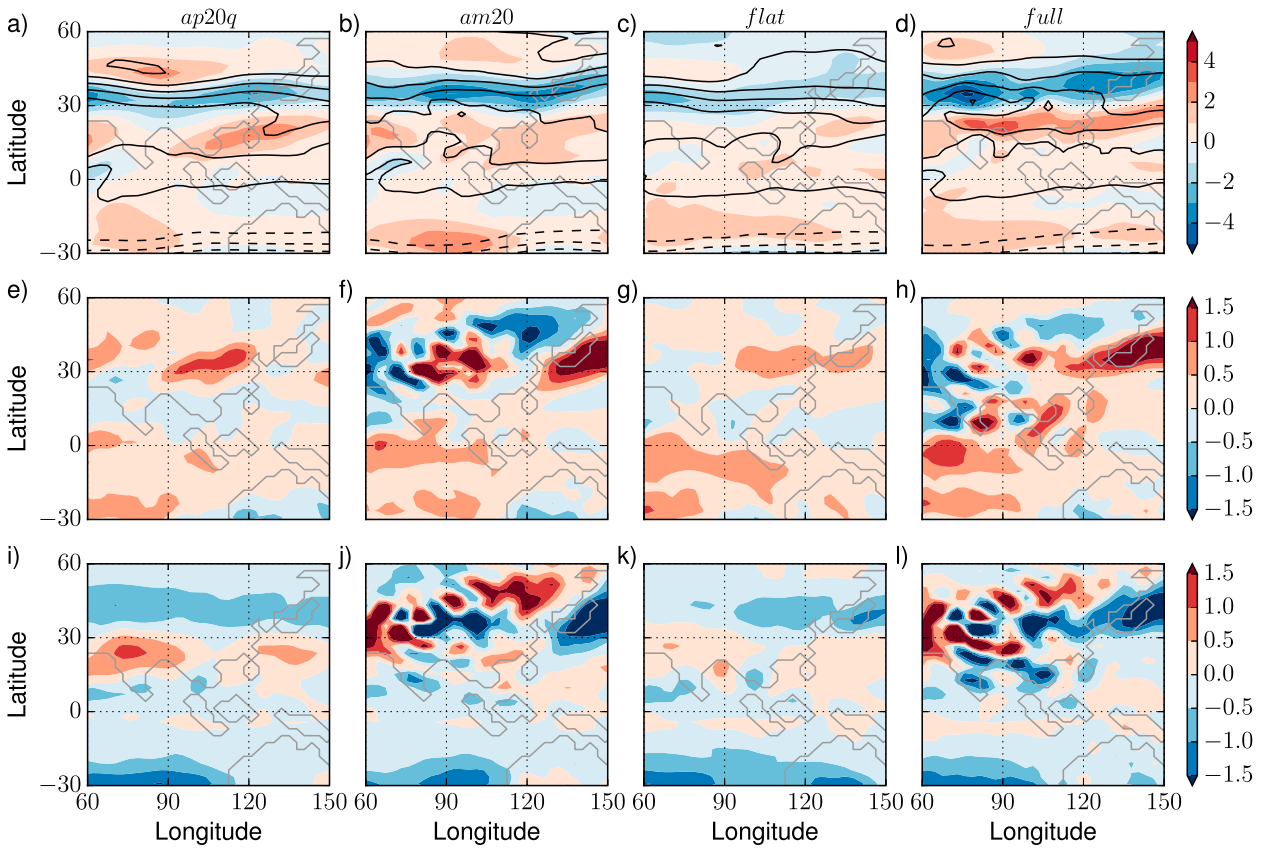


FIG. 12. Vorticity analysis for experiments with nonzonally symmetric surface conditions. (a)–(d) Difference between 150-hPa absolute vorticity averaged over four pentads before and after monsoon onset (day$^{-1}$; color shading). Black contours show the average 150-hPa absolute vorticity after onset, with contour interval 2 day$^{-1}$. Positive and zero contours are solid, and negative contours are dashed. (e)–(h) Average of the vorticity tendency resulting from horizontal advection between 21 April and 15 July (day$^{-2}$); the time between 20-day periods before and after onset used for the nonzonally symmetric experiments throughout the study. (i)–(l) As in (e)–(h), but for the vortex stretching term.

between the am20 and full simulations emerge, with the warming of the Northern Hemisphere appearing to amplify the role of $Q$ fluxes and land. The full experiment now much more resembles a combination of the other experiments. A region of strong geopotential gradient develops over the Pacific coast, similar to that in the experiments without topography. High geopotential gradient is also found over and to the east of the Tibetan Plateau. As this is not evident in either the am20 or flat simulation this feature is assumed to relate to the combination of land and topography resulting in an elevated, warmed region.

As discussed in section 5, the ageostrophic flow increases over onset in the full experiment, showing an enhancement of the circulation beyond that forced by the geopotential gradient. Figure 14 shows the horizontal distribution of this momentum budget term for each of the experiments with a nonzonally symmetric surface. Before onset, southward directed $fv_a$* is seen off the Pacific coast of the continent in all experiments. This flow extends over the continent where topography is included. After onset, significant differences are again seen between the experiments. All experiments show an enhanced southward ageostrophic flow over India, which is significantly stronger when both land and topography are included. Comparing ap20q with the other experiments, it can be seen that $Q$ fluxes alone cannot produce the structure of the southward ageostrophic wind seen along the coast in the other experiments. In this experiment it can be seen that precipitation actually shifts away from the southern edge of the continent after onset, with a northwest–southeast-oriented ITCZ instead intensifying (Fig. 11). In the flat experiment, precipitation and southward ageostrophic wind do develop along the coast, but are weaker and do not extend far to the north. With topography, we see that the am20 simulation develops a stronger ageostrophic circulation over the continental region, and we see again that the combination of land and topography results in an even stronger circulation in the full experiment.

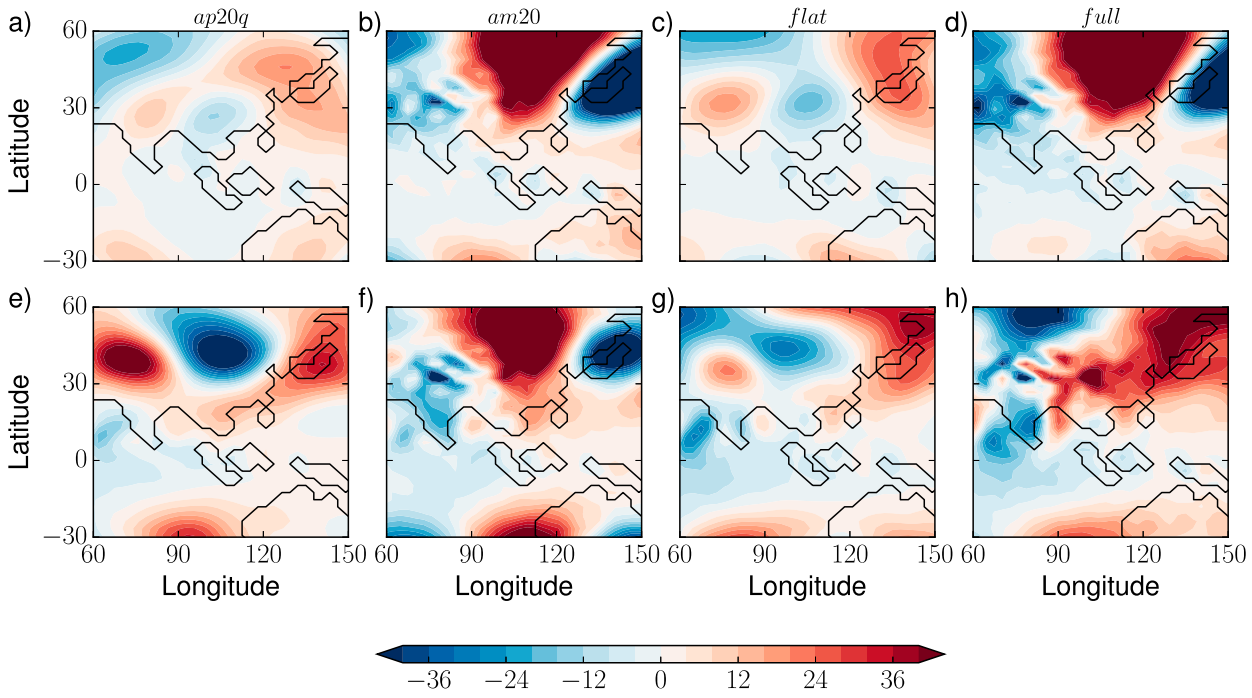


FIG. 13. Spatial distribution of $-\partial\overline{\Phi}^*/\partial x$ at 150 hPa, averaged over 20 days (a)–(d) before and (e)–(h) after monsoon onset. All experiments with nonzonally symmetric surface conditions are plotted.

Figures 13 and 14 lend weight to our conclusions of the previous section. Geopotential gradients related to land–sea contrast and topography develop as the Northern Hemisphere responds to increased insolation, resulting in geostrophic winds and ascent over the continent. These have the additional effects of reducing absolute vorticity over the continent and intensifying the ageostrophic component of the Coriolis force, which is balanced by stationary eddy cross terms. This section emphasizes the importance of topography and land in extending the monsoon system over the entire continent to create the East Asian monsoon, and in strengthening the South Asian monsoon.

## 7. Summary and discussion

Various studies using aquaplanet models have proposed that monsoon onset relates to a change of the tropical circulation from a transient eddy-driven to a thermally direct regime. To investigate the relevance of this perspective to Earth's monsoons, we have performed a range of experiments with an idealized atmosphere model coupled to a slab ocean, with and without a simple description of land.

In both our aquaplanet simulations and in a semi-realistic setup that has an Earth-like distribution of continents, topography, and SSTs (forced by $Q$ fluxes), behavior consistent with a regime change of the Hadley circulation is observed. When the ITCZ shifts sufficiently off the equator, the strength of the cross-equatorial Hadley cell increases, accompanied by a sudden increase in precipitation. In the ap10 experiment, for small excursions of the ITCZ we find that the change in overturning strength per degree latitude can be described by a power law, with exponent $0.09 \pm 0.02$ (Fig. 4). After a threshold latitude of about 7°N is passed, a larger increase in strength with latitude is observed, and the best-fit exponent increases to $0.49 \pm 0.16$. The Student's $t$ test confirms that the two power laws are significantly different at the 95% confidence interval, and that some change in behavior occurs as the ITCZ moves to higher latitudes. Similar relations are obtained for the full experiment, with exponents $0.27 \pm 0.15$ and $0.45 \pm 0.09$, which are again found to be significantly different. The behavior is similar to that of the aquaplanets, particularly in the off-equatorial ITCZ regime, suggesting that similar dynamical processes are at work despite the large differences in the surface boundary conditions between the aquaplanet and full experiments. Whether these exponents have a physical meaning or just act as an indicator of the different relationships between ITCZ latitude and overturning strength remains to be explored via theory.

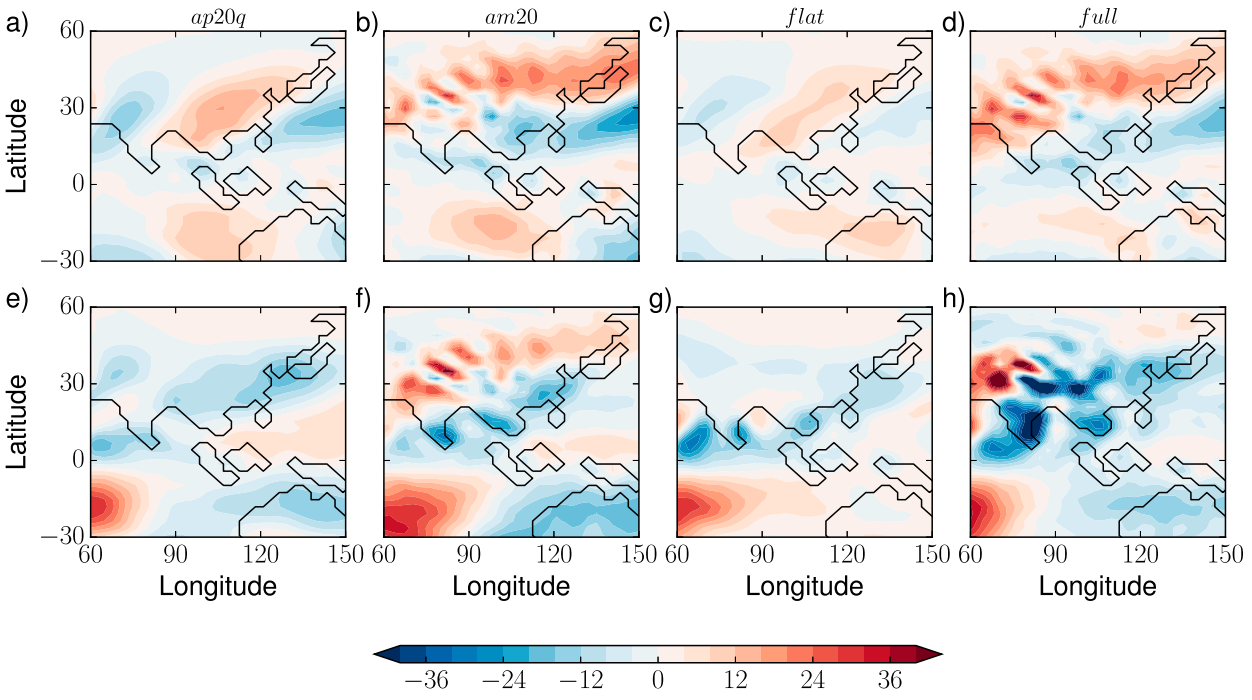


FIG. 14. As in Fig. 13, but for the ageostrophic stationary eddy Coriolis acceleration ($f\overline{v}^* - \partial\overline{\Phi}^*/\partial x$) at 150 hPa.

A consistent feature of the various theories for monsoon onset in idealized studies is a reduction in the magnitude of the upper-level absolute vorticity, which in an aquaplanet suggests a transition to a thermally direct regime [cf. Eq. (1)]. However, the cause of this reduction and the role of zonal asymmetries, and hence the relevance of this result to the real world, has been disputed. Figure 6 shows a schematic summarizing the findings of the present study on the vorticity tendencies in both the equinoctial and monsoon regimes for the aquaplanet case. Our analysis of the upper-level vorticity budget for the ap2 experiment shows that as the ITCZ migrates into the Northern Hemisphere, the magnitude of the vortex stretching term in the budget increases rapidly. This term is the product of divergence and absolute vorticity, and it appears that a regime change is triggered when the region of divergence moves into a region of nonnegligible absolute vorticity. In our simulations this occurs at around 7°N. The circulation shifts toward a thermally direct regime and so strengthens, and the region of ascent broadens. Vortex stretching associated with the ascending air and horizontal advection of vorticity southward across the equator together act as a positive feedback, maintaining and extending a broad region of low-magnitude upper-level absolute vorticity air.

Similar processes are at work in the full experiment, which shows a strong decrease in Northern Hemisphere absolute vorticity centered over the Tibetan Plateau. However, we find that in this simulation warming of the continent, sea surface, and Tibetan Plateau forces a stationary wave and ascent over the plateau. Off-equatorial ascent, so that divergence is collocated with nonnegligible absolute vorticity, again triggers a strong, negative upper-level vortex stretching tendency. The reduced upper-level vorticity helps to move the lower-latitude circulation into a regime with a locally intensified Hadley circulation, which resembles the thermally direct regime in the ap2 experiment. Vortex stretching and horizontal advection of vorticity again act to maintain low absolute vorticity air in the upper troposphere.

The upper-level zonal momentum budget highlights the different natures of the lower- and higher-latitude circulations in the full experiment. North of about 20°N, the flow is predominantly geostrophic. To the south, the ageostrophic flow also strengthens over onset, indicating that the flow is enhanced beyond the component forced by land–sea contrast. We propose that these differently forced elements of the monsoon circulation connect to the East and South Asian monsoon regimes respectively.

These results reconcile some of the apparent disagreement between the regime changes previously discussed. The key process for monsoon onset is demonstrated to be a reduction of upper-level absolute

vorticity, but this may be caused by a variety of mechanisms. Shallow aquaplanets respond strongly to the seasonal cycle, shifting the ITCZ off of the equator and instigating a feedback which lowers absolute vorticity and produces a more thermally direct overturning cell (cf. Bordoni and Schneider 2008). Stationary planetary waves have previously been shown to be able to produce an absolute vorticity reversal, which results in an intensified circulation over areas with a broad region of low absolute vorticity (Shaw 2014). This case is more relevant to our more realistic experiment, where the cyclone that forms over the low pressure region associated with the Tibetan Plateau seems responsible for the onset of a strong cross-equatorial overturning circulation, localized over Asia.

Results from a selection of experiments with different combinations of $Q$ fluxes, land, and topography help to bridge the complexity gap between the aquaplanet and full experiments. In all experiments, as the surface warms over monsoon onset, changes in the geopotential gradient result in ascent over the continent, reduced upper-level absolute vorticity, and changes to the horizontal wind structure. This appears to result in a strengthened ageostrophic component of the meridional wind, similar in some respects to the zonal mean behavior seen in the ap2 simulation. The combination of land and topography appears to be important in advancing monsoon onset and extending the band of precipitation along the southern coast up to the east and over the continent.

This study raises several avenues for future work. While we believe we have identified the mechanism causing the sharp transition during monsoon onset, we do not yet have an analytical theory to describe this process. Additional idealized simulations, both time-varying and steady state, may help in the formulation of this. The role of the Tibetan Plateau in the Asian monsoon systems is still debated (e.g., Boos and Kuang 2010; Wu et al. 2015), and its effect on the regime change, and on East and South Asian monsoon onset, could be explored with some additional simulations. Discussion here has focused on the upper-level circulation. Exploring connections to the energy flux equator framework (e.g., Frierson and Hwang 2012; Donohoe et al. 2013; Hill et al. 2015) might help in understanding how lower-level processes, and consequently choices of model parameterizations, affect the transition. We also hope to investigate the relevance of the regime change processes discussed here to climate change predictions over Asia, by connecting the results of these simulations to data from Earth system models.

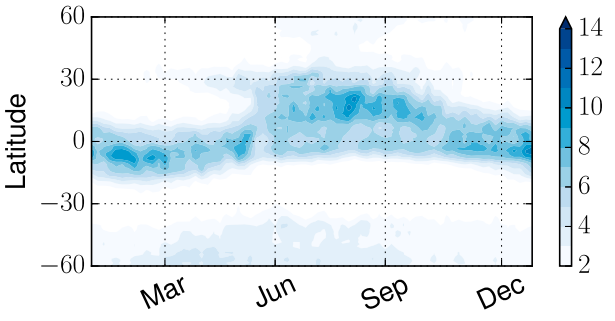


FIG. A1. Seasonal cycle of zonal mean precipitation (mm day$^{-1}$) for GPCP data averaged between 60° and 150°E.

*Acknowledgments.* The work was supported by the UK–China Research and Innovation Partnership Fund, through the Met Office Climate Science for Service Partnership (CSSP) China, as part of the Newton Fund. GKV also acknowledges support from the Royal Society (Wolfson Foundation), the Leverhulme Trust, and NERC (Grant NE/M006123/1). The research materials supporting this publication can be accessed by contacting Ruth Geen (rg419@exeter.ac.uk). We thank Martin Jucker for coupling RRTM to the GFDL idealized model, and Stephen Thomson for many modelling innovations. The comments and insights of our three anonymous reviewers were much appreciated, and improved the final manuscript.

## APPENDIX

### Observational and Reanalysis Data

While the easy to configure and fast to run nature of idealized models makes them useful in exploring dynamical processes, we recognize that they have limitations and should not be assumed to accurately represent the real world. To demonstrate the relevance of the results presented in this study to Earth's climate, we therefore present a selection of figures from the ERA-Interim and GPCP datasets in this section for comparison. Both datasets were linearly detrended. Average climatologies were taken from 1997 to 2014 for GPCP and from 1979 to 2016 for ERA-Interim. Although the details differ in places, the same dynamical features can be seen in the reanalysis data as in the idealized model results discussed above.

The GPCP data (Fig. A1) are broadly similar in structure to the modeled precipitation. Precipitation is slightly more intense in the model than in observations. This likely relates to the idealized convection used in our simulations. Figure A2 shows the

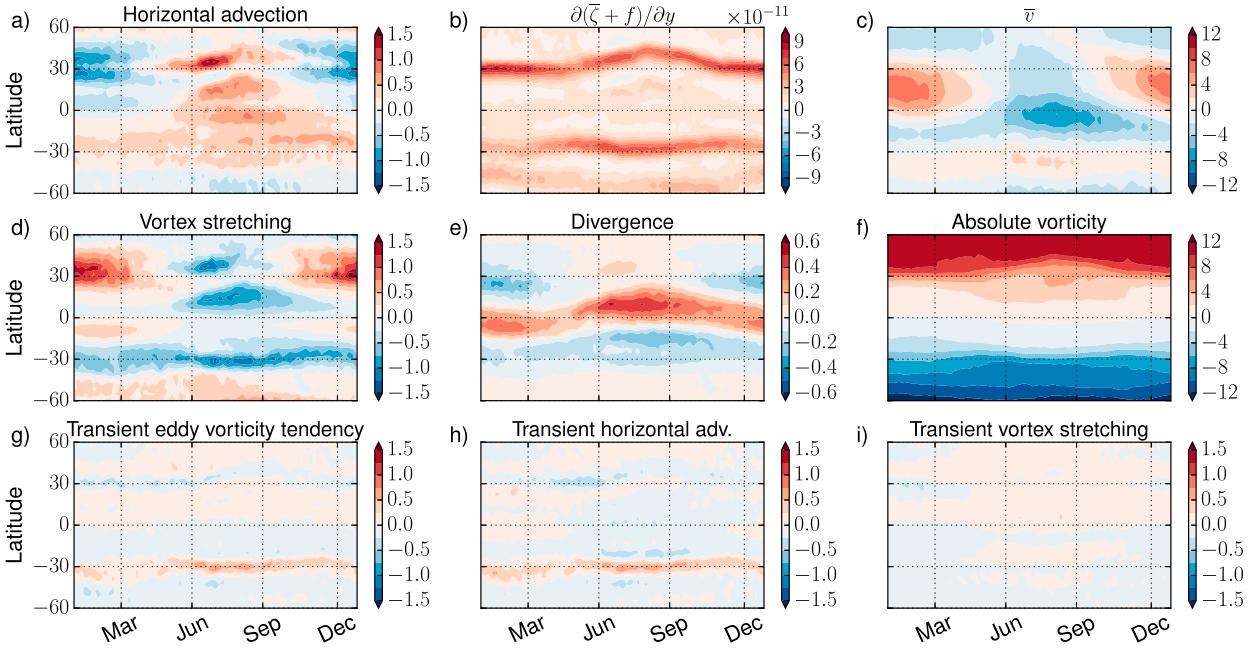


FIG. A2. As in Fig. 7, but for the climatology of ERA-Interim data for 1979–2016.

seasonal cycle of the terms in the vorticity budget for the ERA-Interim data. Notable differences are later arrival of ascent north of 30°N, and no divergence over the equator during Northern Hemisphere summer. However, despite these differences, the reanalysis shows similar behavior to the model, lending weight to our results. Figure A3 shows the seasonal cycle of the terms in the momentum budget for the ERA-Interim data. Again,

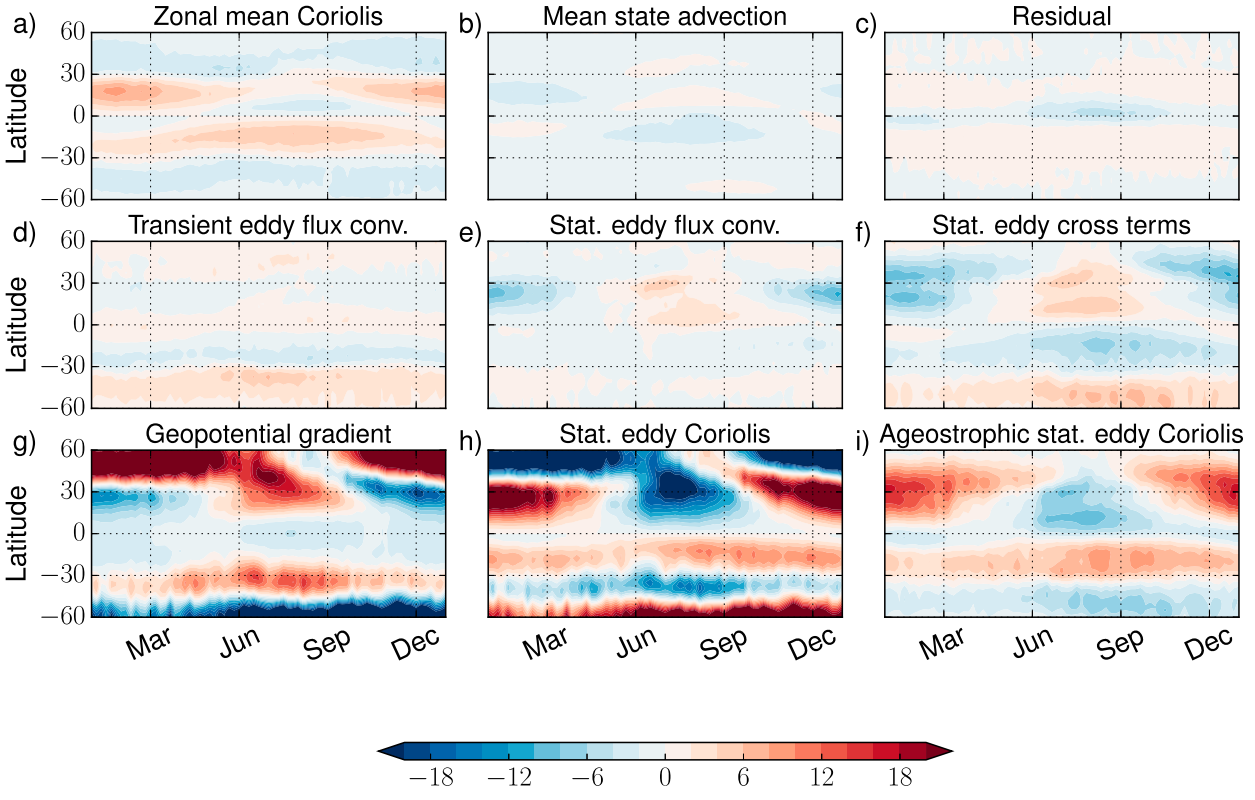


FIG. A3. As in Fig. 9, but for the climatology of ERA-Interim data for 1979–2016.

the behavior is broadly similar. Figures A1–A3 indicate that the mechanisms identified in the idealized model are relevant to the real world.

## REFERENCES


Boos, W. R., and Z. Kuang, 2010: Dominant control of the South Asian monsoon by orographic insulation versus plateau heating. *Nature*, **463**, 218–222, https://doi.org/10.1038/nature08707.

Bordoni, S., and T. Schneider, 2008: Monsoons as eddy-mediated regime transitions of the tropical overturning circulation. *Nat. Geosci.*, **1**, 515–519, https://doi.org/10.1038/ngeo248.

Chao, W. C., 2000: Multiple quasi equilibria of the ITCZ and the origin of monsoon onset. *J. Atmos. Sci.*, **57**, 641–651, https://doi.org/10.1175/1520-0469(2000)057<0641:MQEOTI>2.0.CO;2.

——, and B. Chen, 2001: The origin of monsoons. *J. Atmos. Sci.*, **58**, 3497–3507, https://doi.org/10.1175/1520-0469(2001)058<3497:TOOM>2.0.CO;2.

Donohoe, A., J. Marshall, D. Ferreira, and D. McGee, 2013: The relationship between ITCZ location and cross-equatorial atmospheric heat transport: From the seasonal cycle to the Last Glacial Maximum. *J. Climate*, **26**, 3597–3618, https://doi.org/10.1175/JCLI-D-12-00467.1.

ECMWF, 2009: ERA-Interim, daily. European Centre for Medium-Range Weather Forecasts Public Datasets, accessed 9 June 2017, http://apps.ecmwf.int/datasets/data/interim-full-daily/.

Frierson, D. M. W., 2007: The dynamics of idealized convection schemes and their effect on the zonally averaged tropical circulation. *J. Atmos. Sci.*, **64**, 1959–1976, https://doi.org/10.1175/JAS3935.1.

——, and Y. T. Hwang, 2012: Extratropical influence on ITCZ shifts in slab ocean simulations of global warming. *J. Climate*, **25**, 720–733, https://doi.org/10.1175/JCLI-D-11-00116.1.

——, I. M. Held, and P. Zurita-Gotor, 2006: A gray-radiation aquaplanet moist GCM. Part I: Static stability and eddy scale. *J. Atmos. Sci.*, **63**, 2548–2566, https://doi.org/10.1175/JAS3753.1.

Gill, A. E., 1980: Some simple solutions for heat induced tropical circulation. *Quart. J. Roy. Meteor. Soc.*, **106**, 447–462, https://doi.org/10.1002/qj.49710644905.

Held, I. M., and A. Y. Hou, 1980: Nonlinear axially symmetric circulations in a nearly inviscid atmosphere. *J. Atmos. Sci.*, **37**, 515–533, https://doi.org/10.1175/1520-0469(1980)037<0515:NASCIA>2.0.CO;2.

Hill, S. A., Y. Ming, and I. M. Held, 2015: Mechanisms of forced tropical meridional energy flux change. *J. Climate*, **28**, 1725–1742, https://doi.org/10.1175/JCLI-D-14-00165.1.

Huffman, G. J., D. T. Bolvin, and R. F. Adler, 2016: GPCP version 1.2 one-degree daily precipitation data set. Research Data Archive at the National Center for Atmospheric Research, Computational and Information Systems Laboratory, accessed 13 June 2017, https://doi.org/10.5065/D6D50K46.

Jucker, M., and E. Gerber, 2017: Untangling the annual cycle of the tropical tropopause layer with an idealized moist model. *J. Climate*, **30**, 7339–7358, https://doi.org/10.1175/JCLI-D-17-0127.1.

Kållberg, P., P. Berrisford, B. Hoskins, A. Simmons, S. Uppala, S. Lamy-Thépaut, and R. Hine, 2005: ERA-40 Atlas. ECMWF Re-Analysis Project Report Series 19, 199 pp.

Kim, H.-K., and S. Lee, 2001: Hadley cell dynamics in a primitive equation model. Part II: Nonaxisymmetric flow. *J. Atmos. Sci.*, **58**, 2859–2871, https://doi.org/10.1175/1520-0469(2001)058<2859:HCDIAP>2.0.CO;2.

Krishnamurti, T. N., and Y. Ramanathan, 1982: Sensitivity of the monsoon onset to differential heating. *J. Atmos. Sci.*, **39**, 1290–1306, https://doi.org/10.1175/1520-0469(1982)039<1290:SOTMOT>2.0.CO;2.

Li, C., and M. Yanai, 1996: The onset and interannual variability of the Asian summer monsoon in relation to land–sea thermal contrast. *J. Climate*, **9**, 358–375, https://doi.org/10.1175/1520-0442(1996)009<0358:TOAIVO>2.0.CO;2.

Lindberg, C., and A. J. Broccoli, 1996: Representation of topography in spectral climate models and its effect on simulated precipitation. *J. Climate*, **9**, 2641–2659, https://doi.org/10.1175/1520-0442(1996)009<2641:ROTISC>2.0.CO;2.

Lindzen, R. S., and A. Y. Hou, 1988: Hadley circulations for zonally averaged heating centered off the equator. *J. Atmos. Sci.*, **45**, 2416–2427, https://doi.org/10.1175/1520-0469(1988)045<2416:HCFZAH>2.0.CO;2.

Mlawer, E. J., S. J. Taubman, P. D. Brown, M. J. Iacono, and S. A. Clough, 1997: Radiative transfer for inhomogeneous atmospheres: RRTM, a validated correlated-k model for the longwave. *J. Geophys. Res.*, **102**, 16 663–16 682, https://doi.org/10.1029/97JD00237.

O'Gorman, P. A., and T. Schneider, 2008: The hydrological cycle over a wide range of climates simulated with an idealized GCM. *J. Climate*, **21**, 3815–3832, https://doi.org/10.1175/2007JCLI2065.1.

Peixoto, J. P., and A. H. Oort, 1992: *Physics of Climate.* American Institute of Physics, 520 pp.

Pfeffer, R. L., 1981: Wave–mean flow interactions in the atmosphere. *J. Atmos. Sci.*, **38**, 1340–1359, https://doi.org/10.1175/1520-0469(1981)038<1340:WMFIIT>2.0.CO;2.

Plumb, R. A., and A. Y. Hou, 1992: The response of a zonally symmetric atmosphere to subtropical thermal forcing: Threshold behavior. *J. Atmos. Sci.*, **49**, 1790–1799, https://doi.org/10.1175/1520-0469(1992)049<1790:TROAZS>2.0.CO;2.

Privé, N. C., and R. A. Plumb, 2007a: Monsoon dynamics with interactive forcing. Part I: Axisymmetric studies. *J. Atmos. Sci.*, **64**, 1417–1430, https://doi.org/10.1175/JAS3916.1.

——, and ——, 2007b: Monsoon dynamics with interactive forcing. Part II: Impact of eddies and asymmetric geometries. *J. Atmos. Sci.*, **64**, 1431–1442, https://doi.org/10.1175/JAS3917.1.

Russell, G. L., J. R. Miller, and L.-C. Tsang, 1985: Seasonal oceanic heat transports computed from an atmospheric model. *Dyn. Atmos. Oceans*, **9**, 253–271, https://doi.org/10.1016/0377-0265(85)90022-3.

Schneider, E. K., 1977: Axially symmetric steady-state models of the basic state for instability and climate studies. Part II: Nonlinear calculations. *J. Atmos. Sci.*, **34**, 280–297, https://doi.org/10.1175/1520-0469(1977)034<0280:ASSSMO>2.0.CO;2.

Schneider, T., and S. Bordoni, 2008: Eddy-mediated regime transitions in the seasonal cycle of a Hadley circulation and implications for monsoon dynamics. *J. Atmos. Sci.*, **65**, 915–934, https://doi.org/10.1175/2007JAS2415.1.

Shaw, T. A., 2014: On the role of planetary-scale waves in the abrupt seasonal transition of the Northern Hemisphere general circulation. *J. Atmos. Sci.*, **71**, 1724–1746, https://doi.org/10.1175/JAS-D-13-0137.1.

Vallis, G. K., and Coauthors, 2018: Isca, v1.0: A framework for the global modelling of the atmospheres of Earth and other

planets at varying levels of complexity. *Geophys. Model Dev.*, **11**, 843–859, https://doi.org/10.5194/gmd-11-843-2018.

Wang, H., and M. Ting, 1999: Seasonal cycle of the climatological stationary waves in the NCEP–NCAR reanalysis. *J. Atmos. Sci.*, **56**, 3892–3919, https://doi.org/10.1175/1520-0469(1999)056<3892:SCOTCS>2.0.CO;2.

Wu, G., and Coauthors, 2015: Tibetan Plateau climate dynamics: Recent research progress and outlook. *Natl. Sci. Rev.*, **2**, 100–116, https://doi.org/10.1093/nsr/nwu045.

Wu, R., and B. Wang, 2000: Interannual variability of summer monsoon onset over the western North Pacific and the underlying processes. *J. Climate*, **13**, 2483–2501, https://doi.org/10.1175/1520-0442(2000)013<2483:IVOSMO>2.0.CO;2.

——, and ——, 2001: Multi-stage onset of the summer monsoon over the western North Pacific. *Climate Dyn.*, **17**, 277–289, https://doi.org/10.1007/s003820000118.

Xie, S.-P., and N. Saiki, 1999: Abrupt onset and slow seasonal evolution of summer monsoon in an idealized GCM simulation. *J. Meteor. Soc. Japan*, **77**, 949–968, https://doi.org/10.2151/jmsj1965.77.4_949.

Yin, M. T., 1949: Synoptic-aerologic study of the onset of the summer monsoon over India and Burma. *J. Meteor.*, **6**, 393–400, https://doi.org/10.1175/1520-0469(1949)006<0393:SASOTO>2.0.CO;2.

Zhai, J., and W. Boos, 2015: Regime transitions of cross-equatorial Hadley circulations with zonally asymmetric thermal forcings. *J. Atmos. Sci.*, **72**, 3800–3818, https://doi.org/10.1175/JAS-D-15-0025.1.

Zhang, Y., T. Li, B. Wang, and G. Wu, 2002: Onset of the summer monsoon over the Indochina Peninsula: Climatology and interannual variations. *J. Climate*, **15**, 3206–3221, https://doi.org/10.1175/1520-0442(2002)015<3206:OOTSMO>2.0.CO;2.